Thermodynamics and Kinetics Study of Growth Behavior of Sono-electrodeposited Thin Films

A thesis submitted in partial fulfillment of the requirement for the award of degree of

Masters of Technology
In
Metallurgical and Materials Engineering

Submitted by

Sabita Kumari Rout

Roll No. 208MM107

Department of Metallurgical and Materials Engineering

National Institute of Technology,

Rourkela-769008,

2010

Thermodynamics and Kinetics Study of Growth Behavior of Sono-electrodeposited Thin Films

A thesis submitted in partial fulfillment of the requirement for the award of degree of

Masters of Technology
In
Metallurgical and Materials Engineering

Submitted by

Sabita Kumari Rout
Roll No. 208MM107

Under the Supervision Of

Prof. Archana Mallik **Prof B.C.Ray**

Department of Metallurgical and Materials Engineering
National Institute of Technology,
Rourkela-769008,
2010

National Institute of Technology
Rourkela

Certificate

This is to certify that the thesis entitled **" Thermodynamics and Kinetics study of Growth Behavior of Sono-electrodeposited Thin Films"** submitted by Sabita Kumari Rout in partial fulfillment of the requirements for the award of Masters of Technology in Metallurgical and Materials Engineering with specialization in "Metallurgical and Materials Engineering" at National Institute of Technology, Rourkela (Deemed University) is an authentic work carried out by her under our supervision and guidance.

To the best of our knowledge, the matter embodied in the thesis has not been submitted to any other university/Institute for the award of any Degree or Diploma.

Date -

Supervisor

Prof. Archana Mallik
Metallurgical and Materials Engg.
National Institute of Technology,
Rourkela-769008

Co-Supervisor

Prof. B. C. Ray
Metallurgical and Materials Engg.
National Institute of Technology,
Rourkela-769008

Acknowledgement

I take this opportunity to express my deep regards and sincere gratitude for this valuable, expert guidance rendered to me by guide Prof. Archana Mallik, Assistant Professor, Department of Metallurgical and Materials Engineering, National Institute of Technology, Rourkela and Prof B.C Ray, Professor, Department of Metallurgical and Materials Engineering, National Institute of Technology, Rourkela. I consider me fortunate to have had opportunity to work under their guidance and enrich myself from their vast knowledge and analysis power. They will always be constant source of inspiration for me.

My sincere thanks to Dr. B. B. Verma, Professor and Head Metallurgical and Materials Engineering Department for his talented advice and providing necessary facility for my work.

I would also take this opportunity to express my gratitude and sincere thanks to my honorable teachers for their invaluable advice, constant help, encouragement, inspiration and blessing.

I am also thankful to laboratory members of Department of Metallurgical and Materials Engineering, NIT Rourkela, especially, R. Pattanaik, U. K. Sahu for constant practical assistance and help whenever required.

Special thanks to my husband, parents, friends and other members of the department for being so supportive and helpful in every possible way.

Sabita Kumari Rout

Contents

List of Figures

List of Tables

List of Publications from the Work

1. A. Mallik, **S. Rout**, A. Das: Approaches to understand the non-isothermal grain growth behavior of sono-electrochemically deposited Cu thin film, ***Journal of Applied Physics:*** JR 10-2994 [submitted]

2. **S. Rout**, A. Mallik, B. C. Ray: Thermodynamics and Kinetics study of Growth behavior of Sono-electrodeposited Cu thin films, **3rd National Symposium for Materials Research Scholars MR-10,** 7-8th May, 2010, IIT Bombay, 2010 (Oral presentation).

3. **S. Rout**, A. Mallik, B. C. Ray: Electrochemical Synthesis Of Cu Thin Films Under Ultrasonic Irradiation: The Effect On Ex-situ Growth Behavior, **Recent trends in materials and characterization, 2010,** 14-15th February, 2010, National Institute of Technology, Surathkal, Karnataka, India (Oral presentation).

Publication beyond the scope of current research

1. A. Mallik, A. Das, **S. Rout:** Effect of plating parameters on the magnetic structure distribution in electrodeposited Co/Cu magnetic alloy thin films: An analysis by MFM, ***Journal of Magnetism and Magnetic Materials:*** MAGMAD-10-00544 [submitted]

Abstract

Thin films have wide spread applications like in electronics, optical and magnetic devices and systems because of their improved properties (electrical, magnetic, optical, mechanical) and size reduction as compared to the bulk materials. These films when applied in real applications fail to provide the required properties, if their reliability is affected. Growth of the film is one of the factors which affect their reliability. So the growth behavior in thin films needs concern. In this work we have explored the grain growth phenomena in sono-electrodeposited copper samples.

The samples have been prepared by the above mentioned technique at various (5, 10, 15, 20, 25°C) temperatures. A potential of -300mV was selected for the deposition. Sono-electrodeposition is the modified form of electrodeposition technique. The ultrasound affects the microstructure as well as the adherence of deposit. The phenomenon of cavitation in the presence of ultrasonic field i.e. repeated creation and collapse of the microbubbles at the electrode surface, induces secondary nucleation by crystal fragmentation. Very bright and adherent deposits have been observed after deposition. The investigation of growth behavior in the copper deposits starts by the non-isothermal treatment by Differential Scanning Calorimetry (DSC). The DSC scan is performed from 25-400°C at a temperature ramp of 5, 10, 20°/min. The films are characterized before and after thermal treatment for phase, microstructural and compositional analysis by XRD, SEM, AFM. The surface energies before and after treatment are found by the contact angle measuring instrument. The exothermic peak is observed around 300°C which indicates the occurrence of grain growth. At different heating rates the position of upward peaks shift to higher temperatures indicating growth phenomena is kinetic in nature. To verify the kinetic nature a set of activation energy values have been calculated using Kissinger model. The values varies from 0.8-2.9 eV indicating grain boundary self diffusion growth mechanism. There is variation in surface energy values in treated samples as compared to untreated one, indicates the transition of abnormal grain growth behavior to normal grain growth behavior. The

microstructural analysis also reveals the growth phenomena due to variation of grain sizes between treated and as-deposited samples.

Chapter 1

Introduction

Background
Motivation
Objectives
Thesis outline

1.1 Background

The trend of miniaturization of electronic devices demands the need for thin film materials which replace bulk materials [1]. Thin films are the candidates mainly for the microelectronic devices, solar cells, magnetic devices etc [2-4]. They have gained attention for usage in these devices due to their capability to improve various properties (it may be electrical, magnetic, optical, mechanical properties) which results in increase of efficiency of the devices . Inspite of their upgrade properties, their reliability is an important issue to be concerned. Growth of the film during the service of the device is one of the factors which affect their reliability. As a result of grain growth in thin films, the resistivity decreases, hardness reduces, stress becomes tensile [5, 6]. This initiates various researchers to study the growth phenomena occurring in thin films. There are different synthesis routes to develop these thin films and electrodeposition technique is one among them. It has various advantages over other techniques like potentially very large number of pure metal and alloys can be electrodeposited, easy of control by tailoring the electrodeposition parameters, low processing temperature, deposits onto complex shapes and the production of non-equilibrium materials that cannot be accessed by traditional processes [7-11]. The electrochemical phase formations are usually associated with the nucleation and growth process. The 3D nucleation and growth process includes many stages: diffusion of ions to the electrode, discharge on its surface with resulting ad atoms, critical nuclei formation, crystal growth and overlap as a result of diffusion and ion discharge on the crystal surface and also rearrangement of ad atoms onto a crystal lattice [12-18]. The competitions between these two processes determines the granularity of the deposit [17] and are influenced by the different

operating parameters such as bath composition, pH, bath temperature, over potential, bath additives etc [3, 19-23].

Sono-electrodeposition is the modified form of electrodeposition technique in which electrodeposition occurs in the presence of ultrasonic irradiation. The physical phenomenon responsible for the sono-chemical process is acoustic cavitation, i.e. creation, growth and collapse of micro bubbles. This gives rise to a particular electrochemical reaction. Moreover ultrasound causes ablation of the electrode surface and accelerates mass transport leading to enhanced reaction rates [24-33].

1.2 Motivation

The electrical, mechanical, magnetic and optical properties are affected by the growth of the thin film which in turn affects their reliability. The present work has been carried with an aim to investigate the grain growth behavior in the sono-electrodeposited samples after undergone thermal treatment. The samples have been prepared at different temperatures. Non-isothermal treatment has been done with different heating rates. The Differential Scanning Calorimetry (DSC) serves as the requisite tool for the thermal analysis.

1.3 Objectives

- Electrocrystallization of copper thin films under ultrasound irradiation.
- Characterization of the fabricated films by XRD, SEM, SPM.
- The kinetics of the growth behavior of the films explored by Differential Scanning Calorimetry (DSC).
- Surface energy measurement both before and after DSC by Contact angle measuring instrument.

1.4 Thesis outline

Chapter2 deals the literature beginning with the thin film reliability, including grain growth as one of the factor affecting the reliability of thin films has been elaborately discussed. The different models and modes of grain growth, the sources of stored energy driving grain growth, the mechanism and the laws guiding the grain growth behavior has been focused in this chapter. The growth study in metallic thin films by different researchers has been reviewed. Finally this chapter ends with the basic objectives of the project work.

Chapter 3 focuses on the the brief description of sonoelectrochemistry, the experimental setup, synthesis of the copper thin films and the characterization tools used to characterize the fabricated samples. The electrochemical analysis includes the description of cyclic voltammetry and chronoamperometry. The thermal analysis for the study of growth behavior of the fabricated copper films is done by Differential Scanning Calorimetry (DSC). The phase detection is realized by the understanding of the principle of X-ray diffraction which is carried out by X-ray diffraction (XRD) technique. The topography of the sample surface which can be visualized at high resolution and at high magnification can be understood by the underlying principle in Scanning Electron Microscope (SEM), Atomic Force Microscope (AFM). Finally the study of the surface energy variation in both before and after thermally treated samples is performed by Contact Angle Measuring Instrument (OCA-20 Data Physics).

The Results and Discussions are covered in chapter4. Cyclic Voltammetry and chronoamperometry have been carried out in static and dynamic conditions of the electrolytic solutions at different temperatures. All the information gathered from the voltammograms and current transients are explained and supported by different laws. The phase analysis by XRD provided information about the phases present, particle size and strain in the sample. The topography image by SEM and AFM showed the arrangement of grains, grain size, and roughness of the sample. EDS informed about the composition of the sample. The thermal analysis by DSC provided information about the type of reaction taking place during grain growth (exothermic or endothermic) by upward or downward peak. The quantity of heat release during growth was known from the DSC plots. The dynamic thermal treatment at different heating rates helped to

determine the activation energy for the growth to take place. The surface energy measured by contact angle measuring instrument showed the variation of surface free energy values for as deposited and DSC run samples. Conclusions enlist the detailed results obtained from chapter 4. Finally a list of references has been included, referred for the preparation of the thesis. Whether the proposed growth mechanisms are the way to explore grain growth, will remain unclear until further investigations down to single grain or monolayer films.

Chapter 2

Literature Survey

Thin film reliability
Grain growth effect
The Growth Parable
Techniques for the analysis of grain growth
Investigations of growth behavior on different films

2.1 Thin film reliability:

Coatings were first developed before the arrival of thin films. Coatings (thickness > 1μm) are particularly used for structural applications like as a protective covering over the cutting tools for wear resistance, thermal barrier coatings on turbine blades, protective coating in data storage devices, etc [23,34]. But the thin films (thickness < 1μm) have both structural and functional applications. They are mainly used in electronics, magnetic and optical devices to improve or upgrade their electrical, magnetic and optical properties [2-4]. In all these applications their performance and reliability needs concern. The common failure modes in polycrystalline films are electromigration, oxide breakdown, thermo-mechanical stress, stress induced voids, delamination [35-42]. Electromigration is one of the primary reliability failure mechanisms in ULSI chips. The momentum exchange between conducting electrons and metal atoms cause a net diffusion of metal atoms in the direction of electron flow. The resultant metal flux divergence causes the formation of interconnect voids at the cathode or metal extrusion at the anode. Voiding at the cathode can result in an electrical resistance increase or open circuit in the interconnect line and metal extrusion at the anode can cause an electrical short to the neighbouring lines. The net metal atom flux causes depletion at the cathode and accumulation at the anode [35-37]. This induces severe stresses in both interconnector and surrounding material which increases the rate of growth of pre-existing voids in the solids and also nucleates new voids [36-38].The electromigration resistance can be increased by increase in grain size, grain size uniformity and degree of preferred orientation by appropriate thermal treatment. The thermo-mechanical cycling conditions during processing and service of microelectronic devices cause internal stress to be induced, resulting in

plasticity and creep of the metallic thin films [39]. The stress concentration at the film edges makes edges preferred sites to initiate delamination along film/substrate interface which reduces the adhesion between film and substrate and annealing plays an important role as an adhesion promoter [40-42]. Evolution of grains also tends to affect the reliability of thin films.

2.1.1 Property change due to grain growth:

Various properties such as resistivity, hardness, stress are influenced by the microstructural evolution. It has been reported by various research groups that the resistivity of as-deposited electroplated copper exceeds the bulk value by 10% - 30% but after growth of the film the resistivity decreases to near bulk values, the decrease is about 20% towards bulk value and lowering of Vickers microhardness by 40% [43-45]. Stresses in thin films are classified into two categories, intrinsic and extrinsic stresses. Due to the substantial difference in the thermal expansion coefficient between the film and the thick substrate, thermal stresses are induced in the film due to the thermal treatments during the fabrication or arising later in service are often the cause of failure resulting in decrease of reliability [2].

2.1.1.1 Effect of grain growth on resistivity:

Several mechanisms elucidate the change in resistivity due to increase in grain size. They all introduce scattering events which decrease the electron mean free path from the intrinsic room temperature value of 39nm for single crystal copper which is dominated by phonon scattering [46]. The additional processes include scattering from defects including vacancies, impurity atoms, dislocations, grain boundaries, and second phase particles, plus nonspecular scattering from the top surface, bottom interface, and sidewall interfaces of a copper conductor. To estimate the effect of grain boundary scattering on the resistivity, the model of Mayadas and Shatzkes explains the effects of both surface scattering and grain boundary scattering in polycrystalline metal thin film. The model assumes a random distribution of columnar grains with average grain size G and accounts for the overall decrease in resistivity when the grain size increases. However, the actual grain morphology is somewhat different from this model. The as-deposited grains are smaller than the film thickness. Therefore the film starts with multiple grains in its thickness and some additional scattering is expected from these internal grain boundaries. After the growth of

the grains, the larger grains have diameters much larger than the film thickness, therefore, the time dependence of the resistivity decrease, depends on the morphology of the evolving grains [43, 47]. Fig 2.1 shows the change of resistivity with evolution of grains.

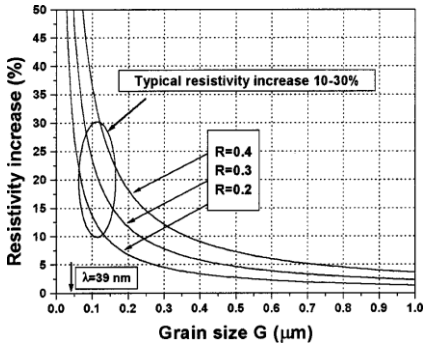

Fig 2.1: Variation of resistivity with grain size

2.1.1.2 Effect of grain growth on mechanical properties:

The flow stress of thin films is generally modeled as the sum of two components determined by thickness and grain size. The film thickness establishes the energy needed to lengthen dislocations during plastic deformations, while the grain size component represents the grain boundary barrier to dislocation motion, and is described by the Hall-Petch relationship [43]

$$\sigma_{gb} = kG^{-1/2} \qquad (2.1)$$

where σ_{gb} is the flow stress, k is a proportional factor, and G is the grain size. It is evident from the equation that increasing the grain size decreases the flow stress in a film of constant thickness. As the grain size increases by about an order of magnitude, the stress decreases to near zero from initially compressive values or become tensile. If the grain size increases, the grain size component of flow stress decreases which suggests a substantial decrease in hardness [43]. Fig 2.2 provides us information about how hardness changes with the room temperature storage time [45]. This is due to the occurrence of grain evolution. The stress change due to the annealing is shown in fig 2.3.

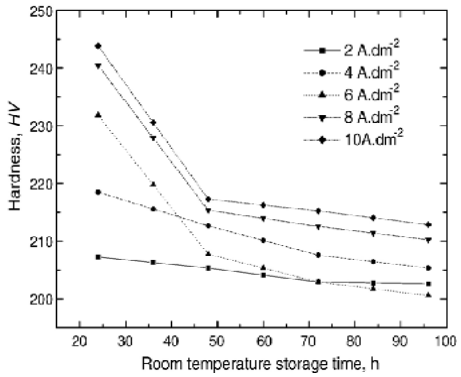

Fig 2.2: Hardness of copper film as a function of room temperature storage time

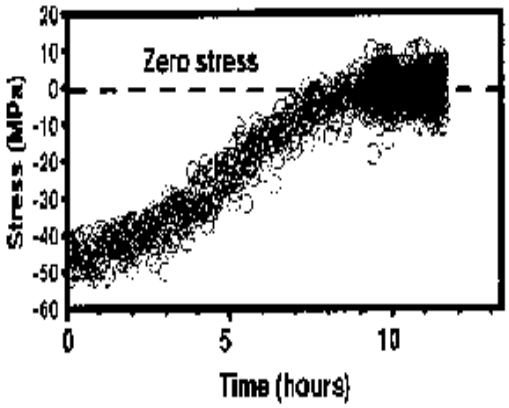

Fig 2.3: The stress change as a function of annealing time

Grain boundaries possess excess free volume per unit area (Δa) when compared to single crystal material. As grains grow, this free volume is redistributed. Thin films attached to thick substrates and having high traction interfaces, results in a biaxial strain given by [48]

$$\varepsilon_d = \Delta a\left(\frac{1}{d} - \frac{1}{d_0}\right) \qquad (2.2)$$

where d is the average grain size at time t and d_0 is the average grain size at t=0. If this strain is elastically accommodated, grain growth can therefore lead to a significant change in the average energy density

$$\Delta F_d = M\,\varepsilon_d^2 \qquad (2.3)$$

where M is the average biaxial modulus. For $d_0 \leq 40A^0$ strain energy density will exceed the energy decrease due to the reduction of total grain boundary energy, otherwise energy driven grain growth is high enough to overcome the high changes in strain energy densities so that grain growth proceeds, leading to increased and potentially high strains [48] as shown in fig 2.4

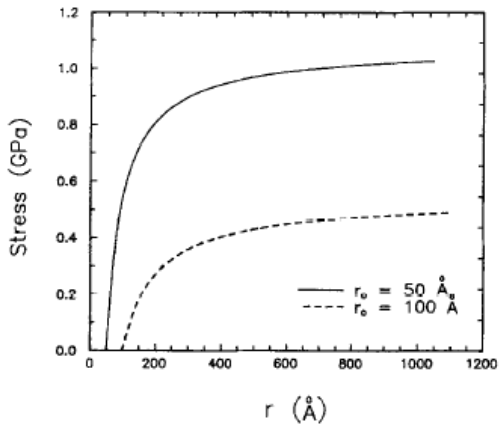

Fig 2.4: Strain resulting from grain boundary-energy-driven grain growth as a function of two initial grain size

The stress change which accompanies the room temperature resistivity decrease indicates a shrinkage or densification of the film with time and can be due to the volume change associated with the loss of grain boundaries. Chaudhari presented a model which assumes that grain boundaries have finite width of material of less than bulk density. This width can be expressed as a layer of missing atoms of width αa, where a is the bulk atom layer spacing and α is a grain boundary parameter (0<α<1). When the thin film, constrained on a substrate, undergoes grain growth then a biaxial stress develops which can be expressed as [43, 49]

$$\sigma = \alpha a E\left(\frac{1}{G_i} - \frac{1}{G_f}\right)/2(1-\upsilon) \qquad (2.4)$$

Where α is grain boundary parameter and lies between 0 and 1, E is the Young's modulus of the film, G_i is the initial grain size, G_f is the final grain size, υ is the poisson's ratio and a is the bulk atom layer spacing.

2.2 The Growth Parable:

2.2.1 Modes of grain growth

Grain growth often occurs during deposition and post deposition processing of thin films. In thin films, grain growth leads to an evolution in the distribution of grain size, and distribution of grain orientations. There exits two modes in which grain growth occurs, they are normal and abnormal grain growth.

2.2.1.1 Normal grain growth

Normal grain growth is taken to be a process in which the average grain size changes with time and is well described by a parabolic law [48, 50-52]

$$D^2 = D_0^2 + Kt \qquad (2.5)$$

where D is the mean grain diameter of each sample annealed at different temperatures, D_0 is the mean grain diameter of the as-deposited film and t is the annealing time. The parameter *K* is written as [50]

$$K = \left(\frac{K'}{T}\right) \exp\left(-\frac{\Delta G^a}{KT}\right) \qquad (2.6)$$

where K' is a constant related with the interface energy density γ. The exp term and the T^{-1} dependence are related with the mobility M of the grain boundary.

It is characterized by the steady state behaviour for which grain size distribution remains monomodal, self similar and has a time invariant shape [48, 53]. In normal grain growth, the grains which are larger than average grain size grow while the grains which are smaller than the

average grain size, shrink or disappear. This results in increase in average grain size, leading to a corresponding decrease in the total grain boundary area. This in turn decreases the energy of the system due to the reduction of the excess free energy associated with grain boundaries. The energy change associated with a change in average in-plane grain size from d_0 to d is [48]

$$\Delta F_{gb} = \gamma_{gb}\left(\frac{2}{d_0} - \frac{2}{d}\right) \qquad (2.7)$$

where γ_{gb} is the excess energy per unit of area grain boundary, d_0 is the initial grain diameter and d is the grain diameter after grain growth. Grain growth resulting in an average grain size that is comparable to the film thickness, normal grain growth usually slows and eventually stops. This is due to the specimen thickness effect. Therefore when normal grain saturates, a completely columnar grain structure develops ie all the grain boundaries intersect both top and bottom surface of the film. According to Mullin, the development of thermal grooves where grain boundaries intersect the surfaces of a film is responsible for the stagnation of normal grain growth [53, 54].

2.2.1.2 Abnormal grain growth

As has been discussed above that as the grains obtain the size comparable to film thickness, grain growth stagnates. Even if, subsequent grain growth is observed it is usually abnormal. In this case, the growth of the sub population of grains is favoured in which small fraction of the population of grains continues to grow while the majority of the grains either donot grow at all or grow at much slower rates. Grain-orientation-specific driving forces for grain growth can arise from several sources. The top and bottom surfaces of thin films have an excess energy per unit area γ_s. For a film on a substrate, the bottom surface will have an excess energy per unit area γ_i. Both γ_i and γ_s depend strongly on the orientation of a grain with respect to the plane of the film. The growth of the grains with γ_s and γ_i minimizing orientations are generally favoured over the growth of grains with other orientations. This can result in the development of bimodal grain size distribution [48, 53] in which the favoured grains grow to sizes that can be many times the film thickness. Mullins proposed that, if the surface energies for grains meeting at a boundary are sufficiently different, the boundary can avoid groove-induced stagnation. In this case low γ_i and γ_s grains grow at the expense of stagnant matrix of grains with other orientations. This mode of

growth is often referred to as secondary grain growth. The change in energy associated with grain-growth-induced reductions in the average surface and interface energy of a film, γ_s and γ_i respectively can be expressed as [48]

$$\Delta F_{s/i} = \frac{\Delta\bar{\gamma}}{h} \qquad (2.8)$$

where $\Delta\bar{\gamma} = [\bar{\gamma}_s - (\bar{\gamma}_s)_0] - [\bar{\gamma}_i - (\bar{\gamma}_i)_0]$

where $\bar{\gamma}$ and $(\bar{\gamma})_0$ are final and initial average energies respectively, h is the film thickness.

Abnormal grain growth may occur when there is an additional driving force for grains to grow beyond the usual limit of normal grain growth or when the normal grain growth process is hindered by particle pinning mechanism [43]. Electroplated copper films undergo spontaneous abnormal grain growth at room temperature, occurring during the first few hours after deposition allowing some grains to initiate abnormal grain growth. The pinning particles evolve along the grain boundaries in the early hours after deposition by the process of Ostwald ripening. Hence the particles coarsen, their average spacing increases and their ability to pin grain boundaries decreases. Eventually certain grain boundaries break free from the pinning sites and undergo abnormal grain growth. The transition from pinned to rapidly moving grain boundaries can be abrupt as the driving pressure is increased (pinning pressure is decreased) therefore we may not easily observe the nucleation sites and be able to identify their specific microstructure. The presence of grains with diameters exceeding the film thickness is a clear signature of abnormal or secondary grain growth [43].The rapid and abrupt grain growth can only be explained in terms of a significant increase of grain boundary mobility. The grain boundary velocity behavior can be expressed as [50]

$$\upsilon = \left(\frac{C\Delta G}{TV_m}\right) \exp\left(-\frac{\Delta G^a}{RT}\right) \qquad (2.9)$$

where C is a constant, R is the gas constant, T is the annealing temperature, ΔG is the difference in free energy between neighbor grains, ΔG^a is the activation energy for atomic migration between grains and V_m is the molar volume.

2.2.2 The growth models

Four different models of arrangement of particles are possible in a solid. Growth can place in any of these arrangements which are thermodynamically favorable. In model-1, a particle is in contact with another particle of twice its size. In model-2, the small particle is placed between two large neighbours. Model-3 and model-4 consist of identical particles and correspond to the particle arrangements in model-1 and model-2 respectively [55]. Fig 2.5 illustrates the four different models of arrangement of particles.

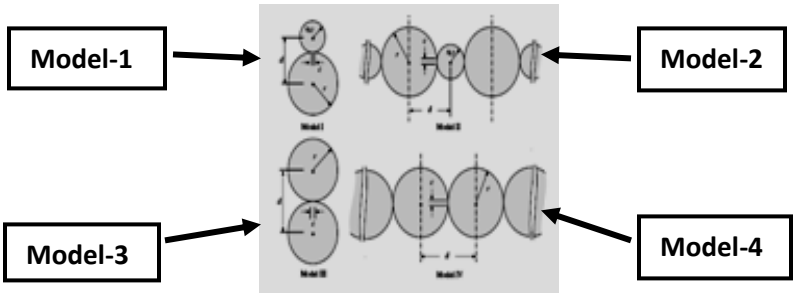

Fig 2.5: Four models of arrangement of particles

2.2.3 Sources driving the grain growth

Microstructural evolution typically involves the movement of grain boundaries within the material. The velocity of grain boundary is expressed as [56]

$$v = M\Delta G \qquad (2.10)$$

where M is the grain boundary mobility and ΔG is the driving force. The driving force for microstructural evolution is related is to different sources of stored energy in the as-deposited film as given in Table 2.1.

Table 2.1: Overview of the estimated driving force ΔG for microstructural evolution related to different sources of stored energy in the as-deposited film [56]

Mechanism	Equation	Assumption	ΔG in J/cm^3
Grain boundaries	$E_{GB} = \frac{3\gamma}{2R}$	R=50nm; γ=0.625J/m^2	~20
Stacking faults	$E_{SF} = \frac{\gamma_{SF}}{nd_{111}}$	n= 3 – 20; γ_{SF}=0.078J/m^2	~125-20
Dislocations	$E_{disl} = \frac{\rho G b^2}{2}$	ρ=10^{12} – 10^{13}/cm^2	~15-140
Surface energy	$E_{surf} = \frac{-2\Delta\gamma}{h}$	h= 500nm	~0.05
Elastic strain	$E_{strain} = \varepsilon^2(F(1,1,1) - F(1,0,0))$	ε = 0.2%	~2
Zener pinning	$E_{Zener} = \frac{-3\gamma\rho_p}{2R}$	ρ_p= 0.2%; r= 0.1nm	~-20

For the atom to make the transition across the grain boundary, it has to cross the energy barrier E_a . The probability for an atom to move from grain A to grain B will be proportional to exp(-E_a/kT) while the probability to move from B to A will be proportional to exp[-(E_a+ΔG)/kT. The net transport will therefore be proportional to exp(-E_a/kT)[1-exp(-ΔG/kT)]. If ΔG ≪ kT then

$$v = \left(\frac{M_0 \exp\left(-\frac{E_a}{kT}\right)}{kT}\right)\Delta G \qquad (2.11)$$

2.2.4 Grain growth mechanism:

There are different mechanisms by which grain growth occurs, such as Ostwald ripening, formation of triple junction grain boundaries, zener pinning effect.

2.2.4.1 Ostwald ripening

Ostwald ripening is the process by which larger particles grow at the expense of smaller ones [57]. When a phase precipitates out of solid, energetic factors will cause large precipitates to grow, drawing material from the smaller precipitates which shrink. This thermodynamically-driven spontaneous process occurs because larger particles are more energetically favored than smaller particles. This is due to the fact that the molecules on the surface of a particle are energetically less stable than the ones already well ordered and packed in the interior. Large particles with their lower surface to volume ratio result in a lower energy state. As the system tries to lower its overall energy, molecules on the surface of a small particle will tend to detach, diffuse and then attach to the surface of larger particle [58, 59]. Therefore the number of smaller particles continues to shrink while larger particles continue to grow. The Ostwald ripening process is determined by the value of the critical radius r_c. If $r > r_c$, the number of molecules in a particle increases, that is the particle grows. If $r < r_c$, the particle shrinks. With several assumptions the critical radius r_c has been found to be equal to the number average radius r_N [60]. Ostwald ripening process has been observed in solid (or liquid) solutions which describes the change of an inhomogeneous structure over time. Fig 2.6 shows the schematic diagram of Ostwald ripening process [58].

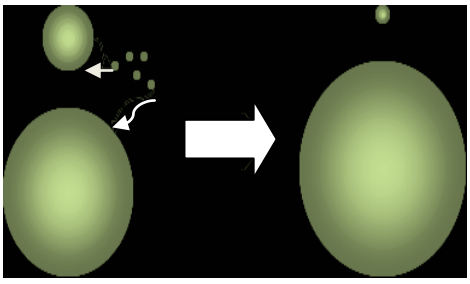

Fig 2.6: Schematic diagram of Ostwald ripening process

2.2.4.2 Triple junction grain boundaries

At the triple point the surface tension forces should be balanced i.e. under the equilibrium conditions, the three grains should meet at angles of 120° at the triple point i.e. the grain should be hexagonal. In order to attain the equilibrium of surface tensions i.e. to make θ =120°, the grain boundaries migrate to bend with simultaneous displacement of the triple point. A curved boundary has more energy, and under the surface tension force, the boundary straightens by moving in the direction of its centre of curvature. The straightening of the boundaries takes place, but which again disturbs the stable equilibrium. This process is repeated again and again resulting in slow disappearance of some grains, while other grains gradually grow. On the whole average size of grains increases. Fig 2.7 shows how grain boundaries migrate towards the centre of curvature to obtain equilibrium angle of 120°, grain 4 is consumed while rest three grains grow [61].

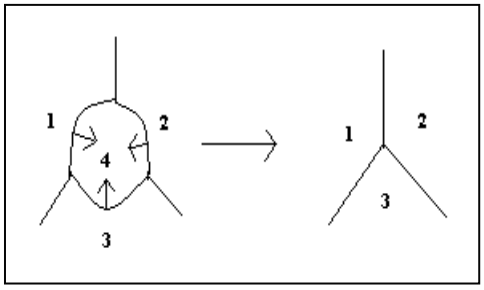

Fig 2.7: Schematic view of how grain growth occurs in order to achieve an equilibrium condition

2.2.4.3 Zener pinning effect

The pinning particles are incorporated from the electroplating bath therefore their volume fraction is fixed by the deposition conditions and the average particle radius at room temperature. This mechanism is consistent with Ostwald ripening of the pinning particles along the grain boundaries in the early hours after deposition. Hence the particles coarsen, their average spacing increases and their ability to pin grain boundaries decreases. Eventually certain grain boundaries break free from the pinning sites and undergo abnormal grain growth. The transition from pinned to rapidly moving grain boundaries can be abrupt as the driving pressure is increased (pinning pressure is

decreased) therefore we may not easily observe the nucleation sites and be able to identify their specific microstructure [43].

2.2.5 Mechanisms controlling grain size:

Zener pinning model of pinning of grain boundaries and grain boundary grooving are the well established mechanism which can cause grain growth stagnation.

2.2.5.1 Zener's model for particle pinning of grain boundaries

Zener modeled the pinning of grain boundaries by second-phase particles and proposed that the particles occupying a grain boundary reduces the overall grain boundary energy by a value given by the obstructed grain boundary area. This value can be expressed as a pressure which opposes the grain growth pressure. The grain growth pressure for normal grain growth is given by [43]

$$P_g = 2\gamma/G \qquad (2.12)$$

where γ is the grain boundary energy density and G is the average grain size. The pinning pressure exerted by the particle according to zener's model is given by [43]

$$P_p = 3f\gamma/2r \qquad (2.13)$$

where f is the particle volume fraction and r is the particle radius. Normal grain growth continues as long as P_g exceeds P_p, but P_g decreases as G increases and eventually the pressures balances each other, resulting in a pinned grain size of

$$G_p = 4r/3f \qquad (2.14)$$

Fig 2.8 depicts how pinned particles along the grain boundaries are restricting grain growth.

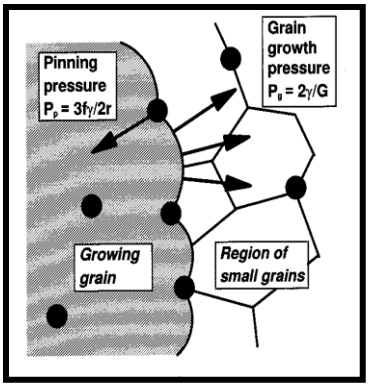

Fig 2.8: Sketch of a growing grain pinned by particles

2.2.5.2 Grain boundary grooving

A common source of grain boundary drag is the formation of grooves where grain boundaries intersect the surface of the film. The motivation for the formation of the groove is the tendency of the grain boundary to shrink in order to reduce its area and hence free energy. The transport processes by which the groove may develop are evaporation, surface diffusion and volume diffusion. If the grain growth is driven by the elimination of grain boundary energy alone, groove formation can result in grain growth stagnation when the average in-plane size is approximately equal to the film thickness [43, 53, 54].

2.3 Techniques for the analysis of grain growth:

The analysis of grain growth both qualitatively and quantitatively can be carried out, first undergoing the thermal analysis by various calorimetric techniques like Differential Scanning Calorimeter (DSC), Differential Thermal Analysis (DTA) and Thermal Gravimetric Analysis (TGA) and then correlated with the corresponding microstructure. Scanning Electron Microscope (SEM) and Atomic Force Microscope (AFM) were the primitive techniques used for the microstructural analysis but currently Transmission electron microscopy (TEM) and Focussed Ion Beam (FIB) images are used to support the thermal analysis. The activation of energy for grain growth can be determined from the information obtained from DSC scans. Various properties like the hardness, resistivity etc affected by the grain growth can be related to their microstructure. Based on this method various researchers have performed experiments to study the thermodynamics and kinetics of grain growth which are enumerated below.

2.4 Investigations of growth behavior on different films

2.4.1 Copper thin films

Copper thin films prepared by Chemical Vapor Deposition (CVD) were studied. The grain size of as deposited film was about 0.1µm. After annealing in an oxygen atmosphere in ambient condition of 1 mTorr, the grains agglomerated with size of agglomerates about 0.5µm. On annealing in vacuum for 24hr, no abrupt change was observed. When oxygen partial pressure was raised to 0.21 atm such as in air, whiskers were formed as shown in Fig 2.9 [62].

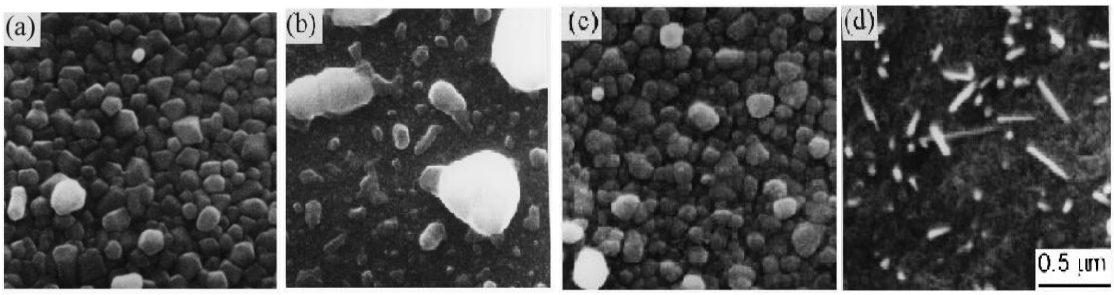

Fig 2.9: SEM micrograph of the surfaces of 150 nm thick Cu films annealed in various ambient (a) as deposited (b) oxygen (450°C, 1mTorr, 30min) (c) Vacuum (d) Air (450°C, 1mTorr, 30min)

2.4.1.1 Copper Selenide thin films

Copper selenide films were produced by vacuum evaporation technique. It was observed that with the increase in annealing temperature (473, 573, 673 °K), the particle size increases whereas strain and dislocation density values decrease with the increase of annealing temperature. From the SEM images it is observed that average smoothness increases with the increase of annealing temperature as shown in Fig 2.10 [63].

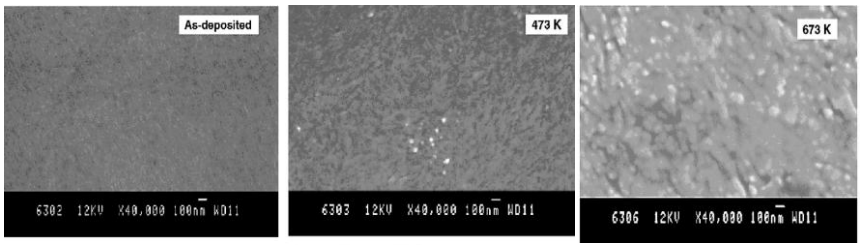

Fig 2.10: SEM micrograph of as deposited and annealed CuSe samples

2.4.1.2 Cu-Cr multilayers

Cu-Cr thin films prepared by magnetron sputtering were studied and it was observed that Cu-Cr thin film when annealed at 630° C showed, the average grain size was 40nm. The interposed chromium layer did not block the copper growth process but were actually ruptured and penetrated by the growing copper grain. The atom motion involved in the copper grain growth occurs along grain boundaries, layer boundaries and free surfaces in thin film multilayer configuration [64].

2.4.2 Silver thin films

Silver films deposited onto quartz substrates by cathodic sputtering showed that the films when annealed in oxygen atmosphere at various temperature between 215°C and 470°C for various periods, caused hillock formation and hole growth. With further heating hole growth continued with final agglomeration is illustrated in Fig 2.11 [65].

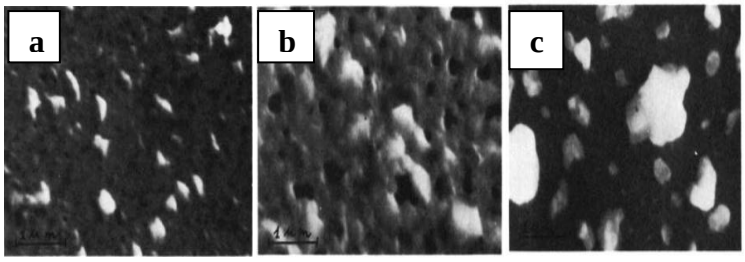

Fig 2.11: SEM micrograph of silver film (a) 1000Å thick heated to 411°C and cooled in oxygen showing hillocks and hole formation (b) 2000Å thick annealed to 470°C for 76 min (c) 500Å thick annealed at 470°C for 2h in oxygen

2.4.2.1 Silver Selenide thin films

Silver selenide films grown on silicon substrates by solid state reaction of Ag and Se when studied, it was observed that on annealing at 373K, the formation of well defined grains with similar shape but with varying sizes were observed along with holes near the grain boundaries. In addition to growth of grains on increase of annealing temperature, there is also increase in the average size of holes and their number density. Annealing at 473K, drastically alters the surface morphology of the deposited film as shown in Fig 2.12. With further increase in annealing temperature the film breaks into islands by forming narrow bridges which may eventually disappear. When annealed at 673K the film agglomerates fully with the formation of island which can be well separated [66].

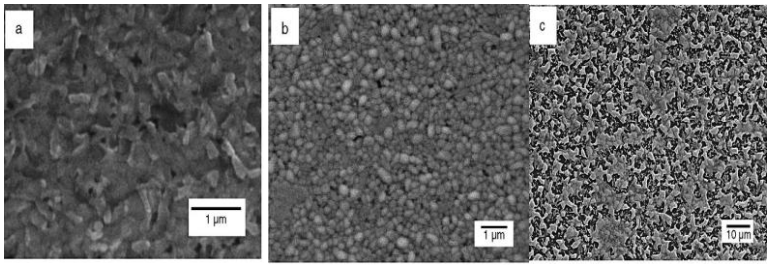

Fig 2.12: SEM micrographs of silver selenide thin films of (a) as deposited and films annealed at (b) 373K (c) 473K

2.4.3 Aluminium thin films

The Al thin film prepared by magnetron sputtering gives rise to the development of mosaic like grain arrangement. It has been reported that annealing treatments in most cases the grain size follows a monomodal distribution. However it has been observed that in some situations the coarsening can take place via abnormal grain growth. A sharp transition from normal to abnormal grain growth occurs within a temperature interval of $\Delta T \approx 13^{o}$ C (The observed phenomenon can be explained in terms of a synergetic grain boundary mobility effect caused by specific characteristics of the nanogranular grain boundary morphology) [50].

The as-deposited sample contains nanograins with mean sizes of ≈30 nm. After annealing, the grains acquire the thickness of the film and present lateral sizes ranging from 0.4 to 1.5 μm. For temperatures up to 450^{0} C the grains present a mosaic-like arrangement preserving the layered

structure from the deposition process. Their growth behavior is rather slow and occurs in both horizontal and vertical directions, being the vertical direction defined as perpendicular to the sample surface. For T ≈ 462^{o}C (i.e. 450^{o}C < T < 475^{o}C), preferential grain growth occurs within the vertical direction, thus leading towards a columnar morphology as shown in Fig 2.14. For T ≥ 475^{o}C the grains grow to a vertical size corresponding to the film thickness and to horizontal dimensions of the order of 1 μm. The conspicuous grain growth behavior observed for T ≥ 475^{o}C can be characterized by a rather rapid horizontal displacement of somewhat vertically oriented grain boundaries as shown in Fig 2.13.

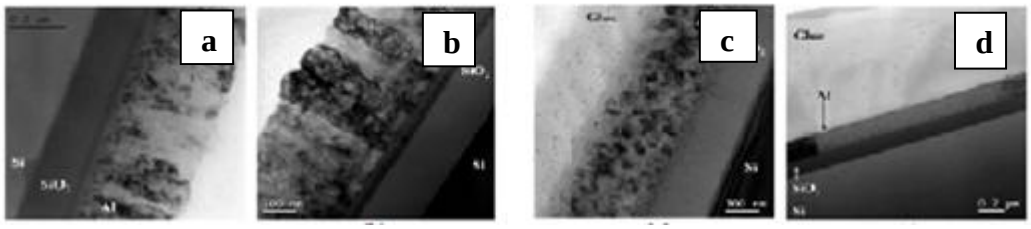

Fig 2.13: Cross-section TEM micrographs showing (a) Columnar-like film as-deposited and (b) Annealed at 500°C for 1hr (c) mosaic-like film as-deposited and (d) annealed at 500°C for 1hr

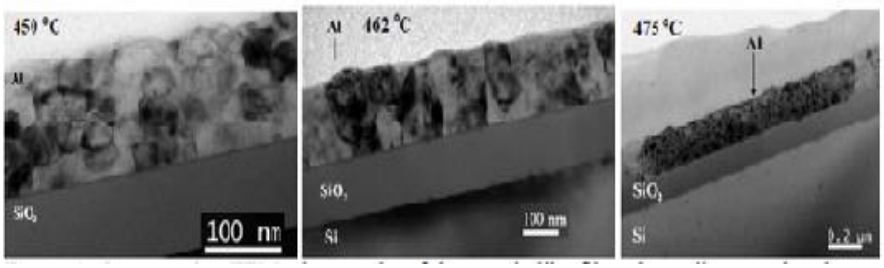

Fig 2.14: Cross-section TEM micrographs of the mosaic-like films thermally treated at the indicated temperature

2.4.3.1 Ti/Al multilayers

Ti/Al multilayers were prepared by d.c magnetron sputtering. Fig 2.15 shows the DSC thermograms of Ti/Al multilayers with 4nm period heated upto 800° C showed two exothermic peaks. The first correspond to the nucleation of the reaction product and coalescence into a continuous layer, the second peak corresponds to the thickening of the TiAl layer [67].

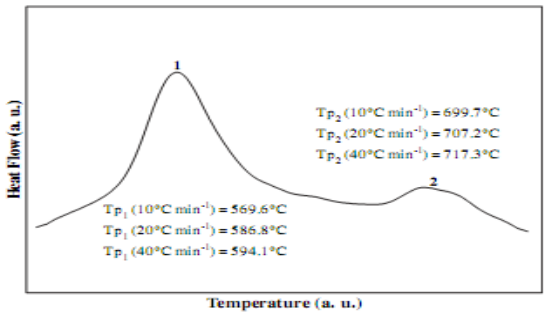

Fig 2.15: Typical DSC curve of Ti-Al multilayer thin film with 4nm period and influence of the heating rate on the peak temperature, T_p

2.4.3.2 Cobalt aluminium bilayers

Co/Al bilayers were prepared by sputtered deposited. After deposition the film were allowed to anneal. After 10 min of annealing at 300°C, as a result of particle impingement a closed Al_9Co_2 phase layers with planar interfaces is formed. The thickness of product layer varies significantly (in the range of ~2-14 nm). These variations emphasize the statistical nature of the nucleation process taking place at this reaction stage. Increase of the annealing temperature results in higher mobilities of atoms or significantly longer times of annealing is required for further thickening of the layer [68].

2.4.4 Nickel films

The nanocrystalline nickel samples were produced by electrodeposition. The annealing studies of nanocrystalline Ni- 1.2wt% P revealed no structural changes at temperature upto 473K whereas at 673K the material transforms rapidly into a microcrystalline structure. At intermediate temperature 573K and 623K, a trasition from initial rapid growth to negligible grain growth of nanocrystalline Ni- 1.2wt% P due to pinning of grain boundaries by nickel phosphide precipitates. The heat released during the grain growth can be detected by Differential Scanning Calorimetry as shown in Fig 2.16.

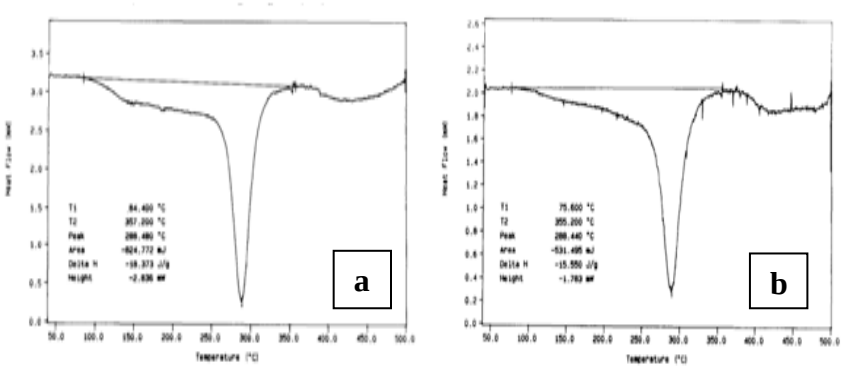

Fig 2.16: DSC scan of Ni sample heating rate 10 K min^{-1} (a) 10 nm size (b) 20 nm size

The DSC scan reveals a superposition of three different processes. The first process causes a broad exothermic reaction which sets in at temperature as low as 353K, leading to a heat heat release of about 25%. The second process is the dominating peak of heat release with an onset temperature of 562K. The third process is the weakest reaction which release heat of about 15% in the 20nm specimen and less pronounced in 10nm Ni sample.

The DSC scans cannot explain the occurrence of abnormal and regular grain growth (for example by two separate growth peaks). To interpret the DSC scans in connection with the change in microstructure, the annealed samples should be investigated by TEM [69].

2.4.4.1 Nickel silicide thin films

Fig 2.17 presents SEM micrographs showing the surface morphologies of NiSi films annealed at 700°C for (a) 10s (b) 20s (c) 30s (d) 40s. Nickel silicide films were deposited by magnetron sputtering in Ar at 3mtorr. Nickel silicide films after annealing at 700°C for 10-20 sec exhibited a relatively large NiSi grain structure with small isolated pinholes and films annealed for ≥30sec showed a complex structure consisting of large grains. Therefore with increasing annealing time the NiSi grain size increases with grain growth accompanied by film agglomeration [70].

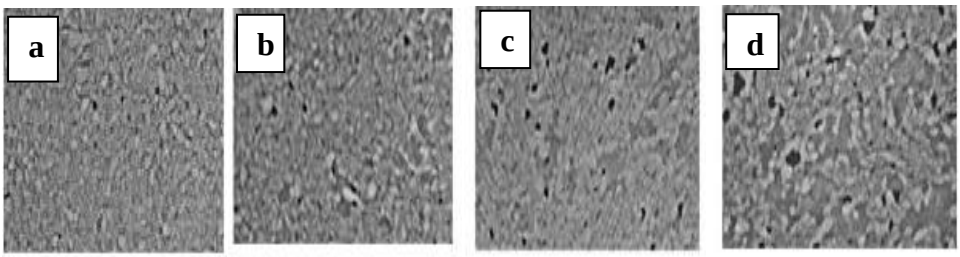

Fig 2.17: SEM micrographs showing the surface morphologies of NiSi films annealed at 700°C for (a) 10s (b) 20s (c) 30s (d) 40s

2.4.5 Cadmium telluride thin films

Fig 2.18 showsDSC trace recorded for the Te layer on Si (heating rate 10 K min^{-1}). An endothermic transition is observed at 435°C which has been attributed to the melting of thin films of tellurium metal. No other peaks were observed over the temperature range studied upto 1000°C [71].

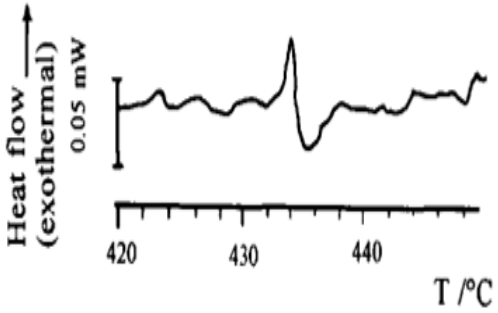

Fig 2.18: DSC trace recorded for the Te layer on Si (heating rate 10 K min^{-1})

2.4.6 Chromium Carbide films

Amorphous films $Cr_{84.8}C_{15.2}$ ($CrC_{0.18}$) were electrodeposited from an electrolyte containing 100 g/l of chromic acid, 5 g/l of sulfuric acid and 30 ml/l of an 85% concentration of formic acid solution. A typical DSC scan of amorphous $Cr_{84.8}C_{15.2}$ ($CrC_{0.18}$) films obtained at a heating rate of 10 K/min is shown in Fig 2.19 (a) . Two distinct exothermic peaks are observed at 655 and 863 K, which are due to the crystallization of b.c.c. α-Cr and h.c.p. Cr_7C_3, respectively. All these transformations are irreversible, no further transformations are detected upon successive heating.

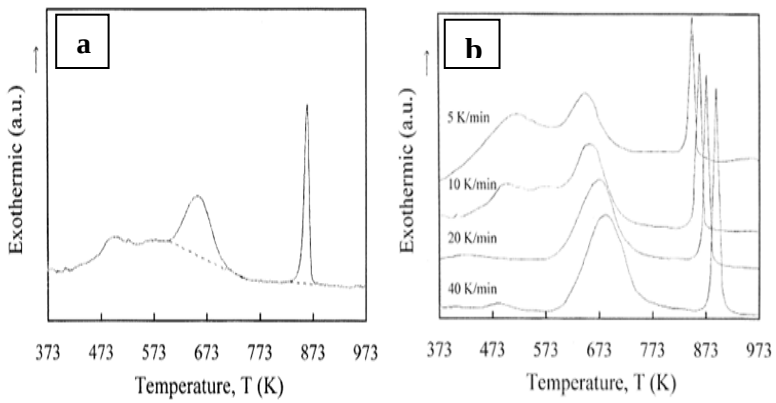

Fig 2.19: DSC scan of electrodeposited amorphous ($CrC_{0.18}$) films at (a) a heating rate of 10K/min (b) different heating rates

Fig 2.19 (b) shows the DSC scans of electrodeposited amorphous (Cr C $_{0.18}$) films at different heating rates. The values of these two crystallization peak temperatures T_{P1} and T_{P2} increases with increasing heating rate α. Two approaches are used to analyze the dependence of crystallization peak temperature T_P on the heating rate α. One is the Ozawa method which is represented as [72].

$$ln\alpha = -\frac{E_c}{RT_P} + B \qquad (2.15)$$

where B is a constant for a given amorphous composition. The effective activation energy E_c of the crystallization process is obtained from the slope of a plot of ln α vs. $1/T_P$. The other approach is the use of Kissinger formula which was originally applied to crystallization studies. The dependence of T_P on α is given by [72].

$$ln\left(\frac{\alpha}{T_P^2}\right) = \frac{-E_C}{RT_p} + B \qquad (2.16)$$

where R is the gas constant, E_c is the effective activation energy , T_P is the crystallization peak temperature, α is the heating rate, B is a constant.

Chapter 3

Experimental Section

Experimental setup
Synthesis of the material
Principles of Sono-electrochemistry
Electrochemical Analysis
Characterization Techniques

3.1 Experimental Setup:

Electrochemical studies or experiments were conducted with a potentiostat/galvanostat (Eco Chemie Netherland, Autolab PGSTAT 12) system having computer interface of GPES software and a system of three electrode electrochemical cell. Experiments were performed on graphite (Asbury, USA) substrate with exposed surface area of $0.25cm^2$. A platinum rod of 0.2 cm diameter and an Ag/AgCl electrode (Eco Chemie, Netherlands) served as counter and reference electrodes respectively. Ultrasound irradiation was accomplished by a 20 kHz ultrasonic horn with 20% output power transducer system (Sonics & Materials, VCF1500) fitted with a titanium tip. For low temperature (in the range of 5°C-25°C) electrochemical studies, sonoelectrodeposition was carried out by placing the electrolytic solution in the refrigerator. The temperature of electrolyte solution was measured with digital thermometer.

3.2 Electrolytic Bath Preparation:

The electrolytic bath contains $CuSO_4.5H_2O$ and 98% conc. H_2SO_4. The purpose of using conc. H_2SO_4 is to make the solution electrically conductive. All chemicals were from commercial sources and were of highest purity available. They were used without further purification.

Solution was prepared from an additive free copper sulphate bath with doubly distilled water at room temperature and under moderate agitation.

3.3 Synthesis:

Sono-electrodeposition ,the technique used for the fabrication of copper thin film. The variation of bath temperature was the operating parameter with copper concentration of 0.1M and 40glt^{-1}free acid. The different bath temperatures at which depositions were performed are 5°C, 10°C, 15°C, 20°C, 25°C. The deposition was carried out at -0.3V for 20seconds.

3.4 Sonoelectrochemistry:

The use of sound energy to enhance electrochemical process is well known. The enhancement is generated through the use of high intensity ultrasound. These operate at frequencies (20KHz-10MHz) to generate high level of acoustic streaming together with cavitation. These lead to extremely high rates of mass transfer. These high rates of mass transfer are only encountered when an electrode is placed close to (< 5mm) the surface of ultrasonic probe [73].

The chemical effects of ultrasound do not come from a direct interaction with molecular species. Instead sonochemistry derives principally from acoustic cavitation: the formation, growth, and implosive collapse of bubbles in liquid. Cavitation serves as a means of concentrating the diffuse energy of sound. It is the underlying phenomenon responsible for sonochemistry. Bubble collapse induced by cavitation produce intense local heating, high pressure and very short lifetimes. These hot spots have temperature of roughly 5000°C, pressure of about 500 atmospheres, heating and cooling rates greater than 10^9K/s. Ultrasound keeps the electrode surface clean and improves mass transport such that uniform electrode reaction occurs across the area of a centimeter-scale electrode, with consequently greater reaction velocity at the electrodes [26, 27, 30]. Ultrasound was also shown to affect metal electrodeposition with benefit to the quality of the deposit, its adhesion and morphology, and also the diminution of brighteners and other additives needed in

silent systems. The effects of ultrasound in a liquid are to cause "acoustic streaming" and/or the formation of cavitation bubbles, depending upon the parameters of ultrasonic power, frequency, sonic source characteristics, and solution phenomena such as viscosity, volatility, and the presence of dissolved gases or other nucleation sites.

3.5 Electrochemical Analysis:

The electrochemical phase formation are analysed by various methods including cyclic voltammetry(CV), linear sweep voltammetry (LSV), chronoamperometry (CA)/chronopotentiometry (CP), double pulse techniques, impedance spectroscopy, voltammetry analysis (differential pulse, square wave, sampled DC, AC 2nd harmonic, differential normal pulse), potentiometric stripping analysis etc. The basic principle of CV and CA are described, as they have been utilised in the analysis and synthesis of the copper thin films.

3.5.1 Cyclic Voltammetry (CV):

The cyclic voltammetry is an efficacious method providing the information about the chemistry of redox couples. The redox couple undergoes two sequential electron transfer reactions which can be confirmed from the two peaks in the voltammogram. In typical cyclic voltammetry, the surface of working electrode is started at a particular voltage with respect to a reference half-cell such as calomel or Ag/AgCl, the electrode voltage is changed to a higher or lower voltage at a linear rate, and finally, the voltage is changed back to the original value at the same linear rate. When the surface becomes sufficiently negative or positive, a solution species may gain electrons from the surface or transfer electrons to the surface. This results in a measurable current in the electrode circuitry. When the voltage cycle is reversed, it is often the case that electron transfer between electrode and chemical species will also be reversed, leading to an "inverse" current peak. These features are illustrated in Fig 3.1. It can provide information on the thermodynamics and kinetics of any transfer reactions, involving both species in solution and species adsorbed at an electrode surface [74, 75].

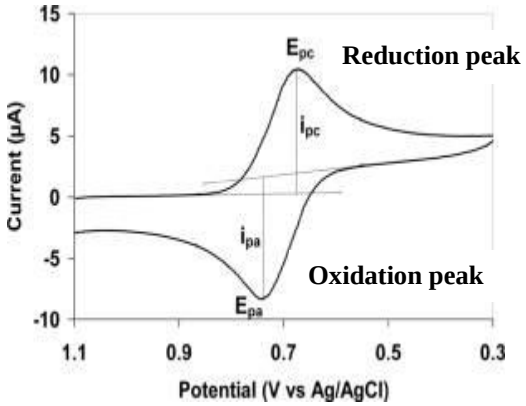

Figure 3.1: A typical cyclic voltammogram showing reduction and oxidation current peaks

3.5.2 Chronoamperometry (CA):

Chronoamperometry (CA) is an electrochemical method in which a step potential is applied and the current, i (A), is measured as a function of time, t (s). This i-t response is comprised of two components: the current due to charging the double-layer and the other due to the electron transfer reaction with the electroactive species. When the working electrode is immersed in the electrolytic solution, a very thin region called the double layer is formed at the electrode-electrolyte interface. The double layer contains a distribution of ions at the interface and is considered to work as a capacitor (C) that represents the electrode double-layer capacitance [76]. The current (i.e., electrons) flows to the working electrode (WE) in order to bring its potential to some desired value. A potentiostat with a 3-electrode cell provides the current via the auxiliary electrode (AE) to the WE while the potential is measured with respect to a reference electrode (RE).

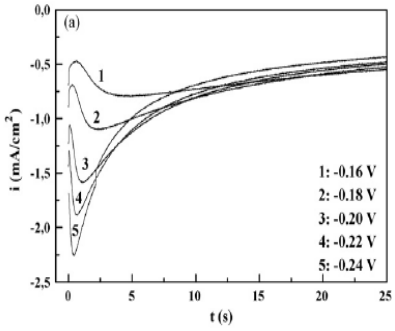

Fig 3.2: Current transients for copper deposition on FTO substrates at different applied potentials

Let us examine now a current, i, vs. time t, response in the presence of an electroactive species that undergoes an electron transfer reaction at a diffusion-controlled rate. Under these conditions, the current decay is given by cottrell law [77]

$$i = \frac{nFD^{1/2}C^{b}}{\pi t^{1/2}} \qquad (3.1)$$

where n is the number of electron(s) transferred per electroactive molecule or ion, F is Faraday's constant, A is the area of the electrode surface in cm^2; D is the diffusion coefficient in cm^2/s; C^b is the concentration of the electroactive species in mol/cm3; and t is time in second. The current rises rapidly to a maximum value decays as a function of $t^{1/2}$, as seen in Fig 3.2.

3.6 Characterization Techniques:

Different experimental techniques were employed to characterize the sono-electrodeposits of copper thin films. The X-ray diffraction was carried out in the range of scanning angle 40°-100° at a scanning rate of 2°/min with CuKα radiation (λ=1.54A^0) using Philips X'Pert system X-ray Diffractometer. The surface topography including the microstructure, grain size, roughness, thickness of the film was analysed using Scanning Electron Microscope (SEM-Jeol 6480LV) and Atomic Force Microscope (AFM-Vecco dilnnova). Energy Dispersive Spectroscopy (EDS) was utilized for the determination of chemical composition/purity of the thin film. The thermal analysis for the study of growth behavior was performed using Differential Scanning Calorimetry(DSC- Mettler Toledo-DSC 822). The surface energy was measured by using Contact Angle Measuring Instrument (OCA-20 Data Physics).

3.6.1 X-ray Diffraction (XRD)

X-ray diffraction is a versatile, non-destructive technique that reveals detailed information about the about the phases present both qualitatively and quantitatively and crystallographic structure. It utilizes the phenomenon of X-ray Diffraction to detect the phases and the structure of the sample.

It is a technique in which analytical results are correlated with references and standards of International Centre for Diffraction Data (ICDD) [78].

3.6.2 Scanning Electron Microscopy (SEM)/ Energy Dispersive Spectroscopy (EDS)

The Scanning Electron Microscope is a type of electron microscope that image the sample surface by scanning it with a high energy beam of electrons in raster scan pattern. The electron interact with the atoms that make up the sample producing signals that contain information about the sample surface topography.These signals include secondary electrons (that produce SEM images), backscattered electrons (BSE), diffracted backscattered electrons (EBSD that are used to determine crystal structures and orientations of minerals), photons (characteristic X-rays that are used for elemental analysis and continuum X-rays), visible light (cathodoluminescence-CL), and heat [79]. EDS is an analytical technique used for the elemental analysis or chemical characterization of a sample. Its characterization capabilities are due in large part to the fundamental principle that each element has a unique atomic structure allowing X-rays that are characteristic of an element's atomic structure to be identified uniquely from one another [79].

3.6.3 Atomic Force Microscopy (AFM)

The atomic force microscope (AFM) is a very high resolution type of scanning probe microscopy with demonstrated resolution of fractions of a nanometer more than 1000 times better than the optical diffraction limit. The AFM is one of the foremost tools for imaging, measuring and manipulating matter at the nanoscale. The information is gathered by “feeling” the surface with a mechanical probe. Piezoelectric elements that facilitate tiny but accurate and precise movement on command enable the very precise scanning [80].

3.6.4 Differential Scanning Calorimetry (DSC)

DSC is a thermoanalytical technique in which the difference in the amount of heat required to increase the temperature of a sample and reference is measured as a function of temperature. Both the sample and reference are maintained at neatly the same temperature throughout the experiment. The reference sample should have a well-defined heat capacity over the range of temperatures to be scanned.

Principle

The basic principle underlying this technique that, when the sample undergoes a physical transformation such as phase transitions, more or less heat will need to flow to it than the reference to maintain both at the same temperature. Whether less or more heat must flow to the sample depends on whether the process is exothermic or endothermic. By observing the difference in heat flow between the sample and reference, Differential Scanning Calorimeters are able to measure the amount of heat absorbed or released during the phase transitions.

DSC curves

The result of a DSC experiment is a curve of heat flux versus temperature. There are two different conventions, exothermic reaction in the sample shown with a positive or negative peak, depending on the kind of technology used in the experiment. This curve can be used to calculate enthalpies of transitions. This is done by integrating the peak corresponding to given transition. The enthalpy of transition can be expressed as [81]

$$\Delta H = KA \qquad (3.2)$$

Where ΔH is the enthalpy of transition, K is the calorimetric constant, A is the area under the curve. Fig 3.3 shows a schematic DSC curve demonstrating the appearance of several common features.

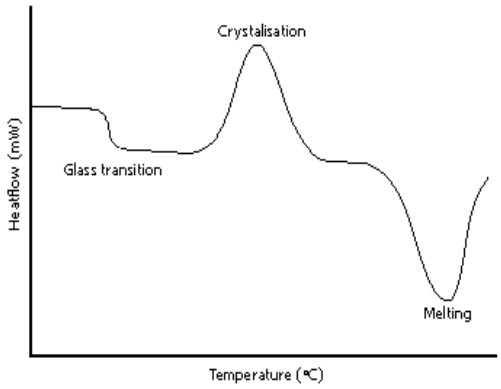

Fig 3.3: A schematic DSC curve demonstrating the appearance of several common features

3.6.5 Contact Angle Measuring Instrument

The device measures the contact angle in static mode which is used for the precise determination of surface or interfacial tension of liquids as well as the surface free energies of solids. In the static contact angle measurement the water drop is allowed to fall on the sample surface. The contact angle is then measured by the software. The smaller the measured contact angle, the better is the wetting between liquid and solid. The device uses upto-date optics, precise mechanics and a high resolution video measuring technique and obtains the right viewing in any measuring situation. The Young-Dupre's equation for the balance of forces in the so called three phase point between liquid, solid and vapour contributes to the measurement of surface free energy of solids.

$$\gamma_{SG} = \gamma_{SL} + \gamma_{LG} cos\theta \qquad (3.3)$$

where γ_{SG}, γ_{SL}, γ_{LG} are the interfacial tensions between the solid and the gas, the solid and the vapour and the liquid and the gas respectively and θ is the contact that the drop makes with the surface [82]. Fig 3.4 illustrates the contact angle between the liquid drop and the rigid surface. The view of water droplet sitting on the deposit is shown in the fig 3.5. Fig 3.6 illustrates the surface energy plot using Owens-Wendt & Kaelble (OW) method.

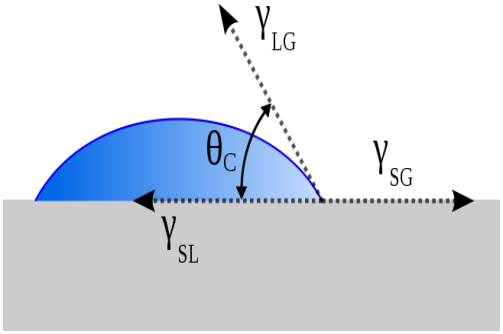

Fig 3.4: Contact angle of a liquid droplet wetted to a rigid solid surface

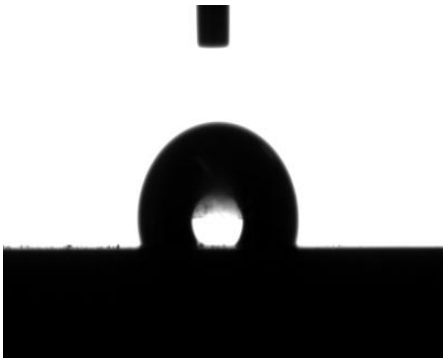

Fig 3.5: The water droplet sitting on the deposit

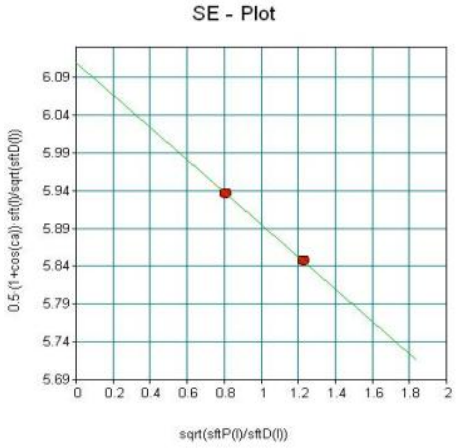

Fig 3.6: The plot for surface energy determination by Owens-Wendt & Kaelble (OW) method

Chapter 4

Results and Discussions

Electrochemical Analysis
Thermal Analysis
Surface Characterization

4.1 Electrochemical analysis:

4.1.1 Cyclic Voltammetry (CV)

Cyclic voltammetry (CV) was carried out under silent and sonicated conditions in the potential range (-0.6V to +0.6V). Fig 4.1 shows CV scans for graphite electrodes at different bath temperatures (5°C, 10°C, 15°C, 20°C, 25°C) performed with a scan rate of 10 mV/s both at static and sonication conditions. In case of silent atmosphere, well resolved anodic and cathodic peaks are visualized. At 20°C, two cathodic and one anodic peaks are observed. The two cathodic peaks is due to the reduction of Cu^{2+} and Cu^{1+} ions and the single anodic peak is due to oxidation of Cu^{2+} ions whereas at other temperatures single reduction and oxidation peaks are observed which is due direct reduction and oxidation of Cu^{+2} ions. It can be observed that deposition of copper starts at potential around -0.01V on the negative potential sweep and then there is increase in cathodic current due to increased availability of copper ions. The cathodic reduction peak appears at a potential of nearly -0.14V. One crossover between anodic and cathodic peaks appears at 5°C whereas for other cases two crossovers are observed. One crossover potential indicates the process may be either charge controlled or mass controlled whereas two crossover potential signifies that the process is both charge and mass controlled. On the reverse scan, the anodic peaks due to the dissolution of copper is observed at a potential nearly +0.28V. In case of sonication as shown in Fig 4.1(b) the anodic peak heights are observed as higher compared to that under static condition. This indicates the increased amount of copper deposition under the effect of ultrasonic irradiation. But the cathodic reduction peaks are not prominent and there exists no

crossover potential. This indicates that it is not mass controlled instead charge controlled and diffusion is enhanced under the effect of ultrasonic irradiation. There is no shift in the oxidation peak except for 5°C but peak height varies with temperature. This may be due to the change in the amount of copper deposited at different temperature and also the variation of adherence of deposits causes the height of oxidation peak to vary. Table 4.1 illustrates the key features of CV for copper deposition under silent and sonication conditions.

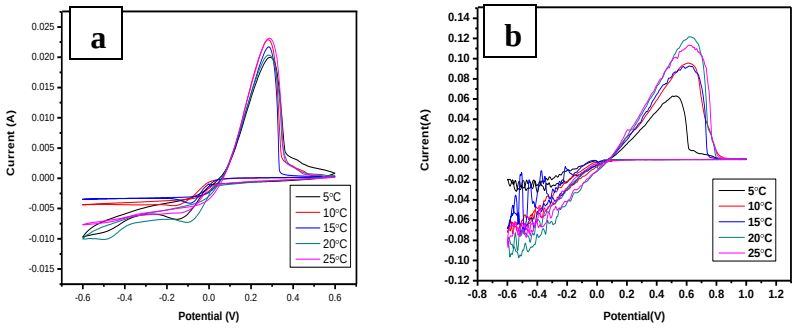

Fig 4.1: Cyclic voltammetry of copper at different bath temperatures in the potential range of - 0.6V to +0.6V under (a) silent (b) sonication conditions

Table 4.1: Key features of CV for Cu deposition under silent and sonicated conditions

Temperature/ °C	Cathodic peak potential/V			Anodic peak potential/V		Cathodic peak height x10^{-4}/A			Anodic peak height x 10^{-2}/A		Cathodic peak area x 10^{-4}/C			Anodic peak area x 10^{-1}/C	
	S*		U#	S	U	S		U	S	U	S		U	S	Ux10^{0}/C
5	-0.146		-	0.292	0.523	-0.049		-	2.015	6.609	0.261		-	3.991	2.226
10	-0.146		-	0.281	0.618	-1.138		-	4.016	9.933	4.255		-	3.526	4.123
15	-0.088		-	0.284	0.618	-6.927		-	2.407	9.388	0.109		-	4.206	3.706
20	-0.091	-0.483	-	0.284	0.635	-3.76	-1.07	-	2.213	12.62	0.186	3.505	-	4.677	5.145
25	-0.122		-	0.288	0.635	-0.839		-	2.648	11.51	5.189		-	5.399	4.816

*Silent, # Ultrasound

4.1.2 Chronoamperometry (CA)

The chronoamperometric curves for copper electrodeposition on the graphite electrode prepared under silent conditions at different temperatures are illustrated in Fig 4.2(a). The current transients were performed at -0.3V for 20 seconds for static and sonication conditions The characteristic feature of the silent deposition curve is the rising current due to the appearance of the new phase and the increasing number of nuclei present on the electrode surface. As these grow, the coalescence of neighboring diffusion fields with the localized spherical symmetry occurs, the hemispherical mass-transfer gives way to linear mass-transfer to the planar electrode surface which is related to the decaying current[18**]** obeying the Cottrell law. At 25˚C the rising current trend is absent which may be due to the sufficient availability of ions at the start of the experiment after which growth of the nuclei occurs which corresponds to the decaying current whereas at other temperatures the rising and decaying current trend is followed. The sonicated chronoamperometric current transients (SCCT) after a two- point Golay-Savitzky normalization are shown in Fig 4.2(b). All the SCCT have a sharp initial decrease in current followed by sequential irregular nucleation and growth loops like current responses. The initial decrease in current corresponds to the double layer charging at the electrode surface. Then the current increases abruptly with a sudden decrease after undergoing a higher and sharper current peak at the maximum compared to that of a silent CCT. The succeeding nucleation loops are the consequences of secondary nucleation due to crystal fragmentation by the formation and collapse of the cavitational bubbles at the electrode surface [83].The SCCTs have the initial loop at around 1.5s and the successive loops have abounded with same time occurrence. The prilimary loops may be due to the conventional 3D nucleation and growth. The current transients are fitted to an Scarrifker and Hills model for the determination of standard kinetics parameters, D(diffusion coefficient) and N_0 (active nucleation density) as shown in Table 4.2. The total charge consumed varies from 0.3-0.5 C as compared to the charges, 0.06-0.09 C involved in the deposition without sonication. The difference may be attributed to the nucleation phenomena. The diffusion coefficient calculated for the silent condition is 0.03-0.04 x 10^{-9} cm^2 s^{-1} while in the presence of ultrasound the value varies from 1.1-3.9 x 10^{-9} cm^2s^{-1}. The diffusion coefficients has increased in presence of ultrasound due to fast mass transport. In the presence of ultrasound the nuclei number density for primary nucleation decreases as compared to silent atmosphere which may be due to the ablation of the electrode surface by the ultrasound, so the number of nuclei near the electrode

surface decreases. The slope of log (current density) vs. log (time) varied from 0.3-0.45 for silent and 0.25-0.35 for sonication, indicates instantaneous phase appearance (not shown).

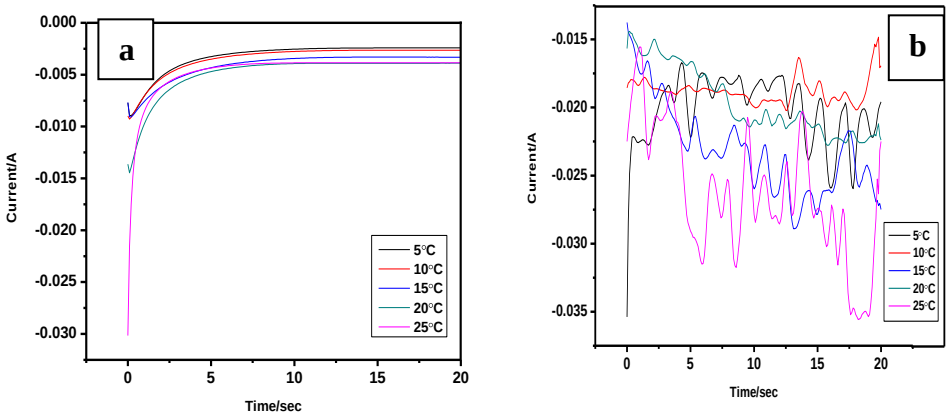

Fig 4.2: Chronoamperometry of copper deposits at -0.3V (a) Silent (b) Ultrasound

Table 4.2: Characteristic kinetic parameters of current transients obtained for silent and sonicated copper deposits

Bath temp (°C)	I_{max} x 10^{-2}(A)		t_{max}(s)		D x 10^{-9} (cm^2 s^{-1})		N x 10^{10} (cm^{-2})		Q_{total}(C)	
	S	US	S	US	S	US	S	US	S	US
5	0.89	2.28	0.1	1.726	0.0325	1.1673	1088.3	4.5604	0.0646	0.406
10	0.92	1.84	0.1	0.885	0.0345	1.2246	1025.5	3.273	0.0689	0.375
15	0.91	1.75	0.1	1.139	0.0384	1.4257	1048	2.1844	0.0822	0.463
20	0.99	1.62	0.1	1.349	0.0401	1.447	885.4	1.8171	0.0916	0.392
25	-	0.0238	-	1.685	-	3.9011	-	0.5396	0.0946	0.530

4.2 Thermal Analysis:

4.2.1 DSC Analysis

The non iso-thermal treatment was performed with electrodeposited copper thin films. Fig 4.3 (a) shows the thermograph of electrodeposited samples after 72 hours annealed at scanning rate of 5°/min from 25 - 400 °C. All the DSC traces exhibit single exothermic crystallization peak. The exothermic peak signifies the occurrence of grain growth where due to the average increase of the grain size decreases the grain boundary area or the grain boundary energy. This decrease of grain

boundary energy can be confirmed from heat release during the exothermic reaction which is supported by the upward peak (exothermic peak) during the thermal scan [43, 48, 84].The exothermic peak starts from 335.3 ℃, 336.5 ℃, 309.37 ℃, 350.63 ℃, 320.84 ℃, reaching the peak differential heat flow at 367.2 ℃, 368.28 ℃, 359.99 ℃, 353.37 ℃, 341.15 ℃ and then heat release decreases gradually up to 400℃ for bath temperatures 5 ℃, 10 ℃, 15 ℃, 20 ℃, 25 ℃ respectively. The peak temperature and the associated heat release are higher for 5℃ as compared to other temperatures. This is because majority of the grains are small sized, so require higher temperature for their growth in comparison to samples prepared at higher bath temperatures where grain sizes increases with increase of bath temperature and so they require less temperature for their grain growth. The growth of the grains must have occurred either between neighboring grains of same size or different size (Ostwald ripening) or by the formation of triple junction grain boundaries. This is verified by the microstructural analysis (SEM, AFM) which will be discussed in the next session. The kinetics of grain growth is qualitatively analyzed by determination of the activation energy values. For its estimation, the samples were heated at different heating rates (5, 10, 20˚/min) and the resulting thermograph is shown in Fig 4.4. The peak temperatures of the exothermic reactions in the DSC signals at different heating rates are applied to the Kissinger model. The relationship between the activation energy and the peak temperature of the exothermic reaction can be described by the following equation [85-87]

$$\frac{E\Phi}{RT_m} = An(1-x)_m^{n-1} e^{-E/RT_m} \qquad (4.1)$$

where E is the activation energy, R is the gas constant, T_m is the peak temperature, Φ is the constant rate of temperature rise, x is the fraction reacted, A is a constant, n is the empirical order of reaction. The activation energy is obtained from the slope of plot of $\ln(\Phi/T_m^2)$ versus $(1/T_m)$ as shown in Fig 4.6 . As illustrated in Fig 4.4, the exothermic peaks of crystallization shift to higher temperature gradually with increasing heating rate. This observation reveals that the growth behavior is kinetic in nature. At low heating rates, the attainment of orientation controlled growth equilibrium contributing to the exothermic heat release is slow, while at high heating rates the grains attain the equilibrium quickly and then grow in random orientation because of lack of any order requiring positive temperature shift compared to low heating rates [88]. So the peak temperature for the high heating rates is generally greater than for low heating rates. The

calculated activation energies are given in Table 3.3. The values signify a grain boundary self diffusion growth mechanism as observed by various authors [44, 53, 89]. This variation of the activation energy might be attributed to the grain size and orientation even though it is not known how they can induce such fluctuations. Each thermal analysis was scanned at least twice to ensure authenticity. No definitive answer can be found at this point. Along with exothermic peaks some unsystematic endothermic peaks have also been observed for 10 °C and 25 °C at various heating rates. The energy consumed for these depressions in the DSC scan can possibly be due to the reaction of nitrogen (the reacting atmosphere in the DSC furnace) with the carbon substrate resulting in an amorphous product during DSC experimentation [90]. The presence of nitrogen in the samples after DSC run was confirmed from the EDS compositional analysis as shown in Fig 4.5. Another set of DSC scan was carried out for freshly prepared deposits at a temperature ramp of 5°/min as shown in Fig 4.3 (b).

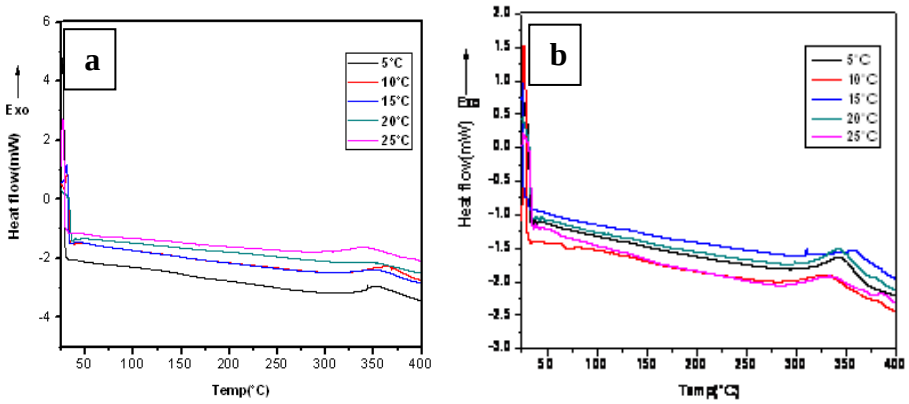

Fig 4.3: DSC scans of copper deposited at different temperatures (a) after 72 hrs annealed (b) as-deposited at scan rate of 5°/min from 25°C - 400°C

Two exothermic peaks have been observed for 25, 15, 20°C which can be supported by the surface energy values. To elucidate the growth mode for the grain boundary driven self diffusion growth, a set of surface energy analysis was done before and after DSC treatment and are given in Table 4.3. Surface energy was found to be increased for temperatures 25, 20 and 15 °C whereas for the other temperatures there is a decrease of the values. The above discrepancy may be attributed to a transition from abnormal grain growth to normal growth with reduction of temperature, which can be correlated with the multi peak observations in the DSC scan for the above temperatures as shown in Fig 4.3(b). And the abnormality in the growth behavior could

rely upon the size difference of the grains in the film due to the crystal breakage induced by ultrasound [83]. The size difference in the grains will reduce as the primary grains gets finer at low temperatures. Hence, the tendency of secondary grain growth would have minimized. These growth kinetic observations are then correlated with structural evolution to envisage and explain the issues further.

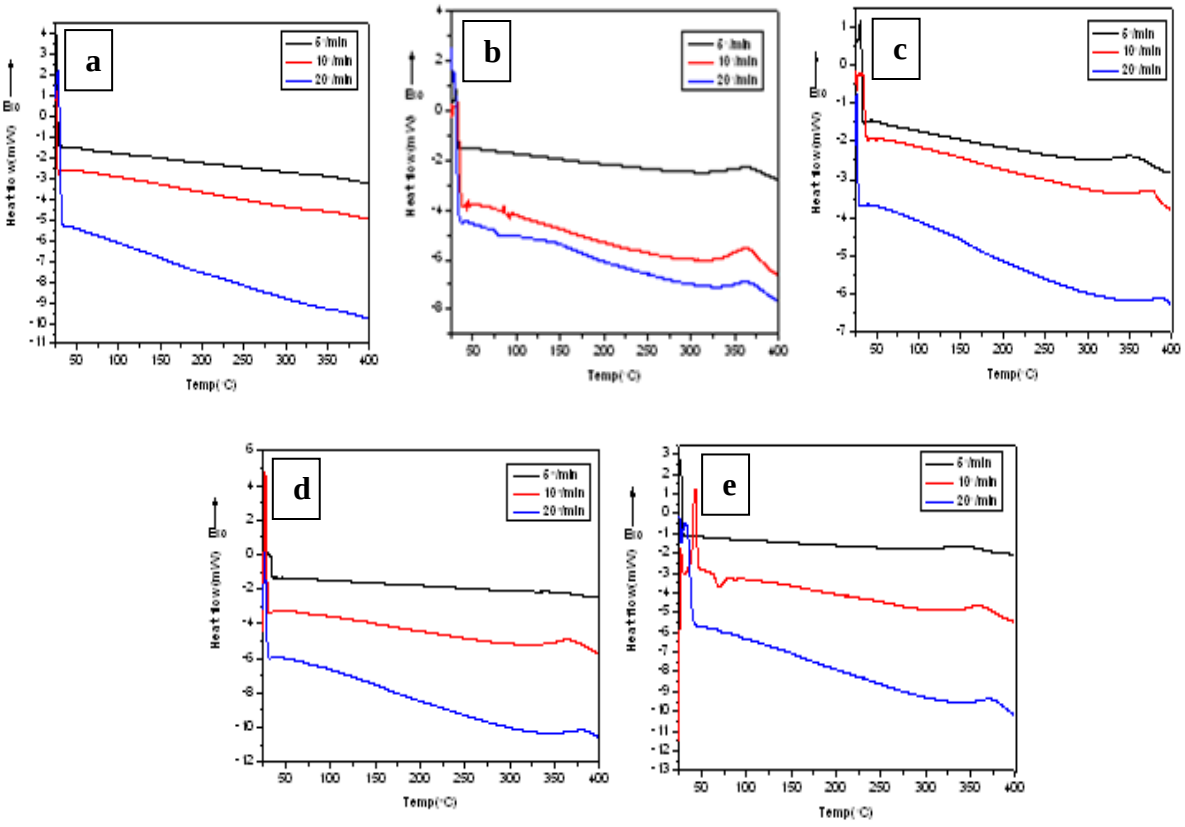

Fig 4.4: DSC scans at heating rate of 5°/min, 10°/min, 20°/min of copper electrodeposited at (a) 5°C (b) 10°C (c) 15°C (d) 20°C (e) 25°C

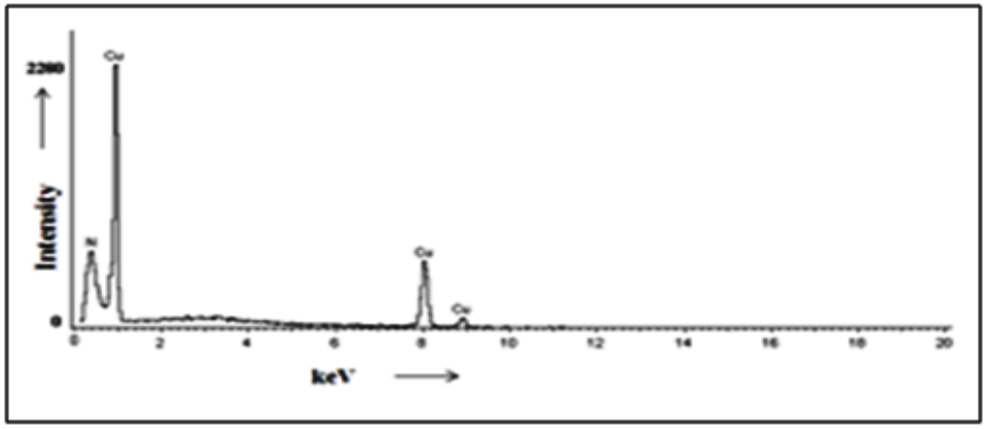

Fig 4.5: EDS plot for post treated DSC copper film

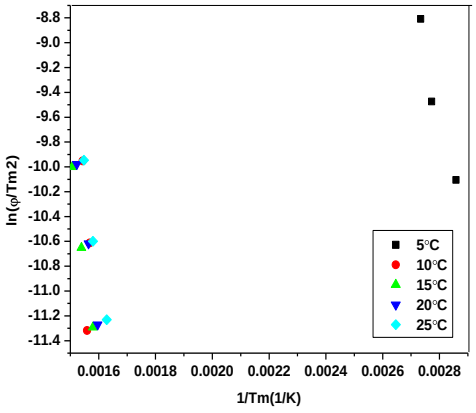

Fig 4.6: Kissinger plot for the calculation of activation energy for an atomic diffusion process

Table 4.3: Activation and surface energies calculated for grain growth for copper deposits at different temperatures

Copper deposition at (°C)	Activation energy (eV/atom)	Surface Energy (mN/m)	
		Before DSC	After DSC
5	0.85	59.92	55.62
10	2.90	51.58	34.24
15	1.51	45.84	67.86
20	1.50	41.77	43.21
25	1.35	30.48	32.30

4.3 Surface Characterization:

4.3.1 Phase Analysis

The XRD patterns of the as-deposited and after DSC scan of copper films have been illustrated in Fig 4.7. Decrease in either domain size or lattice strain will cause effective broadening of diffracted peaks. The Average crystallite sizes of copper deposit were determined by the Williamson-Hall formula [91] (As Scherrer equation is valid only for powders or loosely bound deposits but not for hard and adherent deposits).

$$\beta_{total} cos\theta = \frac{0.9\lambda}{t} + 4sin\theta(\frac{\Delta d}{d}) \qquad (4.2)$$

The sharp peaks show the crystallinity of the copper deposits. The diffraction peaks at 2θ = 43.27, 50.34, 74.12, 89.93 can be indexed as the (111), (200), (022), (311) planes of copper with cubic symmetry respectively (ICDD: 01-085-1326) [92]. The intensity of peaks decreases with decrease in bath temperature as shown in Fig 4.7 (a). This attributes to the formation of smaller sized grains at lower bath temperature compared to the higher one. But after thermal treatment peaks corresponding to copper have been found to have reduced to narrow intensity and have shifted towards left of 2θ (from 43.27° to 43.436° for Cu(111)) values to that of observed values in case of as-deposited copper. The reason for the inverted growth is not clear, but this may be the consequence of the strain developed due to the growth of the grain. The β value has decreased after DSC as the grain size has increased due to grain growth at elevated temperature. Table 4.4 shows the crystallite size and strain calculated from the XRD plots by using the Williamson- Hall formula. It was not possible to calculate the grain size of the treated films deposited at 10 and 5 °C temperatures because of the very low intensity of copper peaks.

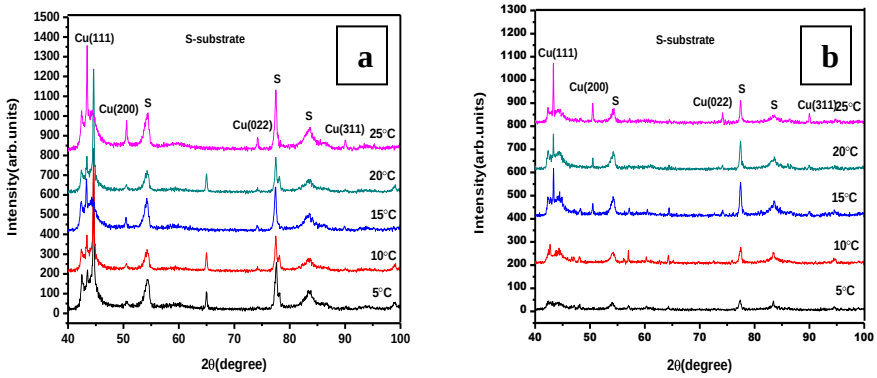

Fig 4.7: XRD patterns of copper deposits under sonication condition (a) before DSC (b) after DSC

Table 4.4: Calculated crystallite size and strain from XRD plots of copper deposits before and after DSC

Bath temperature (°C)	Size (nm)		Strain x 10^{-3}	
	Before DSC	After DSC	Before DSC	After DSC
5	12.4	-	5.50	-
10	22.3	-	4.07	-
15	63.1	140.1	2.12	1.58
20	55.5	138.9	1.81	0.21
25	123.7	166.5	0.27	~0

4.3.2 Structural Analysis:

Fig 4.8 shows the SEM topographies of copper deposits under sonication condition at -0.3V prepared at different bath temperatures. The deposited copper nuclei bear the spherical shape with varying grain distribution (Fig 4.8 a-e). The size of grains decreases with decreasing bath temperature. Due to the effect of intense ultrasonic irradiation and high level of supersaturation at low temperatures, agglomerated copper spheroids of size in between 400 nm to 1 µm are formed. However, the spheroids consist of nano-sized (20-30 nm) agglomerates with an increased extent at reducing temperatures as confirmed by AFM studies, discussed later. Hence the increased

aggregation tendency with finer morphology may lead to better surface coverage resulting firm and adherent morphology. These understandings can be made clear by the fact that, in the presence of ultrasound the crystal fragmentation might have nucleated a large number of copper grains. Moreover, copper is a highly reactive metal having good tendency towards agglomeration. Along with the enhancement in the mass transport due to cavitation, ultrasound also generates shock waves during the formation and collapse cycle. And the generated shock wave may further assist the agglomeration mechanism. Now concentrating on the SEM micrographs (Fig 4.9 f-j), of the samples heated up to 400 °C at a temperature ramp of 5°/min. From the images it can be visualized that after the thermal treatment, grains are bigger than their untreated counterparts with blurred grain boundaries. The distinct features of the surfaces of the treated films prepared at 25, 20 and 15 °C are a bimodal grain distribution, small grains of 100 to 200 nm are observed on the very large grains. Whereas the low temperature films after DSC treatments have nearly uniform grain distributions on the surfaces. To enumerate the above observations, a detail study was done by AFM. For the film prepared at 25°C the growth of the grains of same size in sequence (model-4, discussed in section 2.2.2) and two grains of different size (model-1) has been distinctly observed. The growth of the grains following model-1 has also been observed in 20°C.

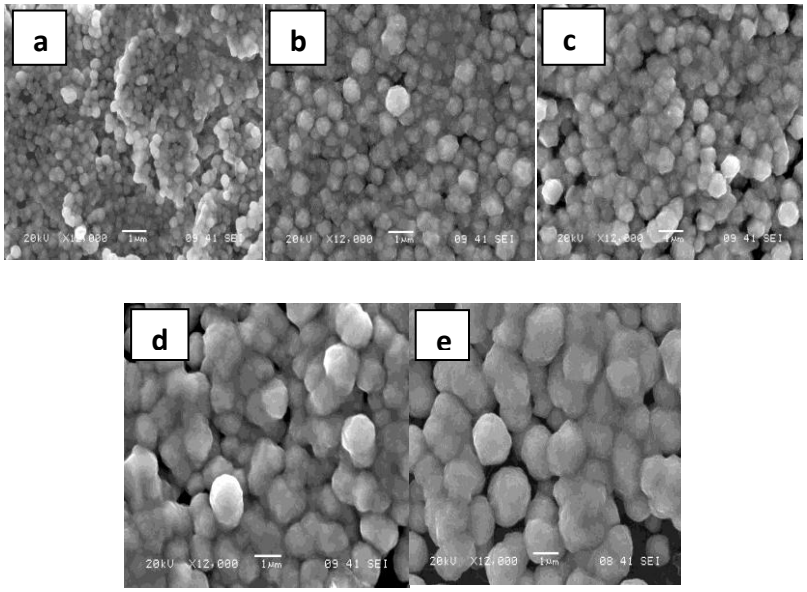

Fig 4.8: SEM images of copper deposits at -0.3V at (a) 5°C (b) 10°C (c) 15°C (d) 20°C (e) 25°C under ultrasonic condition

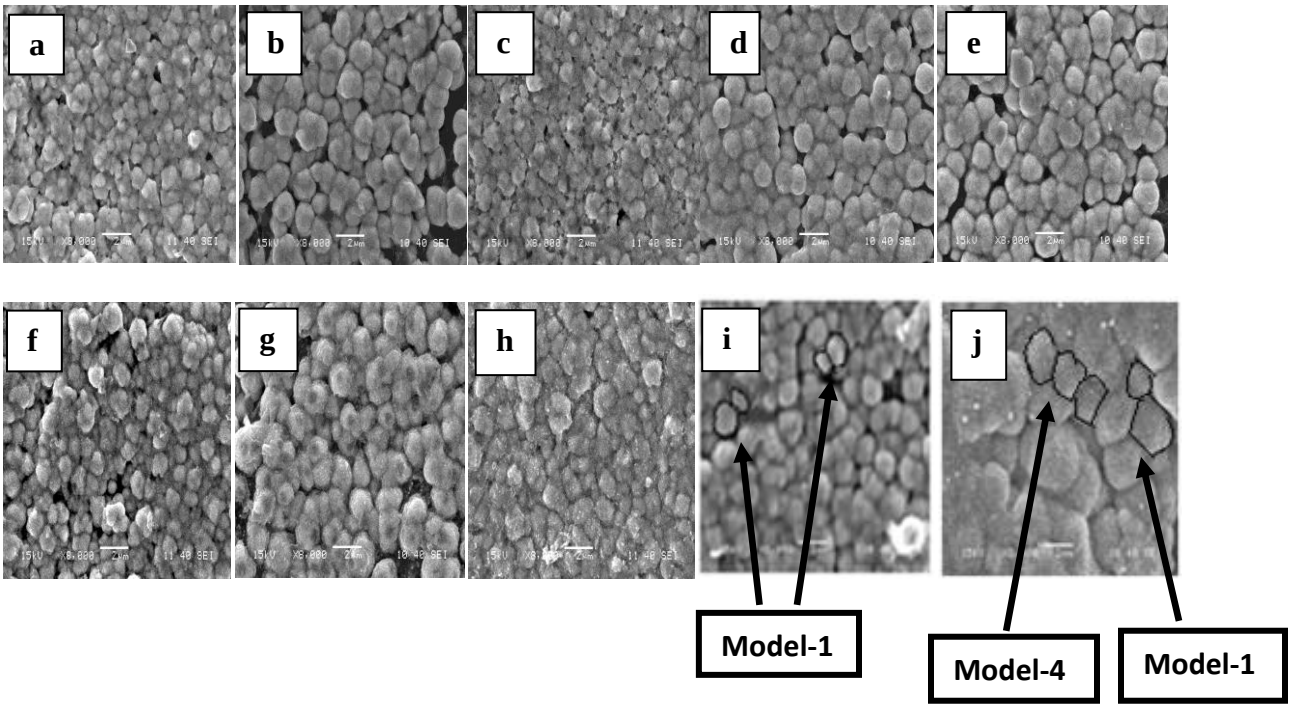

Fig 4.9: SEM images of as-deposited copper at (a) 5°C (b) 10°C (c) 15°C (d) 20°C (e) 25°C and (f) – (j) after DSC at heating rate of 5°/min

However, the SEM studies were not capable of producing the morphological details. Hence structural characteristics are further ventured with AFM. Fig 4.10 presents AFM micrograph of sonicated deposits prepared at different temperatures. The micrographs clearly visualize the agglomerated copper spheroids placed on the host grains which were not clearly identified in SEM micrographs. These agglomerates are the result of secondary nucleation initiated due to crystal fragmentation by the cavitaion phenomena induced by ultrasonic radiation. The agglomerates are seen to be finer for lower temperatures as compared to higher ones. This attributes to the dual effect of supersaturation as well as ultrasonic irradiation at low temperatures. Fig 4.11 represents the AFM micrograph of the deposits after the dynamic thermal treatment at 5°/min. The size of agglomerates is seen to be increased after the treatment as compared to that of the untreated samples signifies the occurrence of grain growth. The roughness factors and the maximum and minimum elevation for copper deposits are illustrated in Table 4.5. The roughness values of the treated surfaces vary from 771 to 135 nm while for as-deposited roughness lies between . The possible reasons can be conjectured at this point: the abnormal growth of fine grained smooth layer has not happened for films deposited at low temperature because of nominal size variations in the primary and secondary grains in as-deposited film.

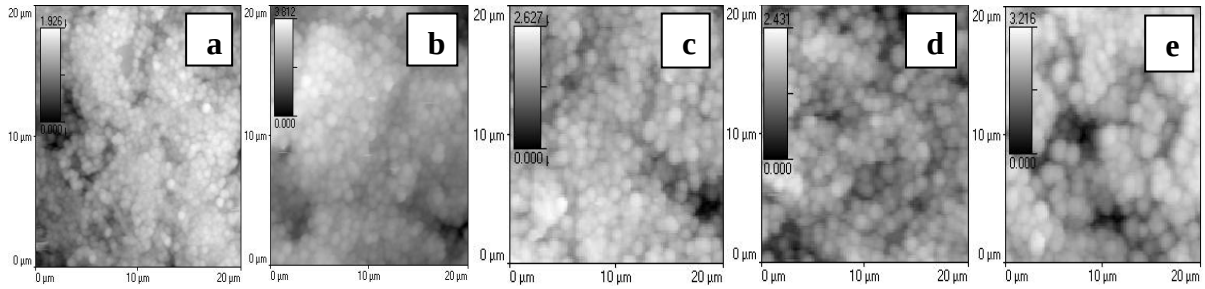

Fig 4.10: AFM micrograph of sonicated deposits at (a) 5°C (b) 10°C (c) 15°C (d) 20°C (e) 25°C

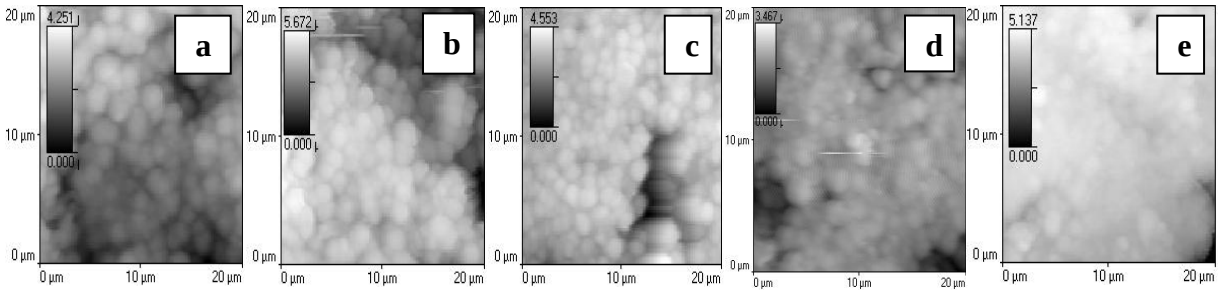

Fig 4.11: AFM micrographs of after thermally treated copper deposits at 5°/min prepared at (a) 5°C (b) 10°C (c) 15°C (d) 20°C (e) 25°C

Table 4.5: Roughness factors and average and maximum heights for copper deposits at different temperatures

Deposition temperature (°C)	Roughness factor (µm)		Average height (µm)		Maximum height (µm)	
	As-deposited	After DSC	As-deposited	After DSC	As-deposited	After DSC
5	0.475	0.771	2.246	2.626	3.811	4.856
10	0.256	0.911	1.261	3.653	1.926	5.671
15	0.369	0.444	1.768	4.017	3.407	4.552
20	0.418	0.286	2.132	1.905	3.216	3.466
25	0.260	0.135	1.335	4.176	2.431	5.317

Chapter 5

Conclusions

On action alone by thy interest, Never on its fruits,
Let not the fruits of action be thy motive, Nor by thy attachment to inaction

Sri Bhagavad Gita, Chapter 2, Versa 47

Copper thin films were prepared from an aqueous solution containing $CuSO_4.5H_2O$ ($6.35gl^{-1}$) and H_2SO_4 ($40gl^{-1}$) on as received fresh graphite substrates under the effect of ultrasonic vibrations in the bath. The depositions were carried out at − 300mV at different temperatures of the electrolyte. The fabricated film was heated from 25 - 400°C at rate of 5, 10, 20°/min with the help of Differential Scanning Calorimeter (DSC) to study the thermal effect on the electrodeposited copper films. The deposits were characterized for phase analysis by X-ray Diffraction (XRD), the morphological analysis by Scanning Electron Microscope (SEM) and Atomic Force Microscope (AFM), compositional analysis by Energy Dispersive Spectrometer (EDS). The surface free energy values were obtained by Contact Angle Measuring Instrument (OCA-20 Data Physics).

The observations and analysis of the results gained from the above studies are enumerated below

1. Cyclic Voltammetry (CV) was performed in the potential range of (-0.6 to +0.6 and +1) V at different bath temperatures to know the chemistry of redox couples both in silent and under ultrasound respectively. The redox couple undergoes two sequential electron transfer reactions which are confirmed from the two peaks in the voltammogram. The cathodic and anodic peaks for silent condition are observed around -0.14V and -0.24V respectively. At 5 and 20°C two reduction peaks are observed which may be due to the reduction of both $Cu^{2+}$and Cu^{1+}ions and one oxidation peak due to oxidation of Cu^{2+} ions. An over potential of 300mV was chosen for the deposition at various temperatures. At

sonication reduction peak is not well resolved, indicates enhanced mass transport by the ultrasound but the oxidation peak is well resolved.

2. Chronoamperometry was performed at −300mV for 20 seconds. The standard kinetic parameters using Scarrifker and Hills model are found. The diffusion coefficients calculated for the silent condition is between 0.03-0.04 x 10^{-9} cm^2 s^{-1} while in the presence of ultrasound the value varies from 1.1-3.9 x 10^{-9} cm^2s^{-1}. The increase in diffusion coefficient in sonication is the consequence of enhanced mass transport by the cavitation phenomena in the presence of ultrasonic field.
3. To explore the growth phenomena in the post non-isothermally treated copper thin film, the study was started by heating the deposits from 25 - 400 °C at heating rate of 5, 10, 20 °C by DSC. The entire DSC traces exhibit either one or two exothermic heat release peaks at around temperature of 300 °C. The exothermic peak signifies the occurrence of grain growth. The peak temperature and the associated heat release are higher for 5 °C as compared to other temperatures for a specific heating rate. This is because majority of the grains are small sized, so require higher temperature for their growth in comparison to samples prepared at higher bath temperatures where grain sizes increases with increase of bath temperature and so they require less temperature for their grain growth. With increasing heating rate the exothermic peak for a particular bath temperature has shifted to a higher temperature. This may be attributed to the attainment of orientation controlled growth equilibrium quickly and then growing in disorder manner, requires positive shift in temperature as compared to low heating rates. Along with exothermic peaks some unsystematic endothermic peaks have also been observed for 10 and 25 °C at various heating rates. The energy consumed for these depressions in the DSC scan can possibly be due to the reaction of nitrogen (the reacting atmosphere in the DSC furnace) with the carbon substrate resulting in an amorphous product during DSC experimentation. The presence of nitrogen in the samples after DSC run was confirmed from the EDS. The activation energies for grain growth are calculated using Kissinger model and lies between 0.85 - 2.9 eV suggesting grain boundary self diffusion occurring during the grain growth process.

4. The growth behavior of the films was found by measurement of surface energy and correlating the data with DSC and morphological results. Surface energy was found to be increased for temperatures 25, 20 and 15 °C whereas for the other temperatures there is a decrease of the values. The above discrepancy may be attributed to a transition from abnormal grain growth to normal growth with reduction of temperature, which can be correlated with the multi peak observations in the DSC scan for the above temperatures. And the abnormality in the growth behavior could rely upon the size difference of the grains in the film due to the crystal breakage induced by ultrasound

5. From the XRD patterns, the diffraction peaks are observed at 2θ = 43.27, 50.34, 74.12, 89.93 are indexed as (111), (200), (022), (311) respectively (ICDD: 01-085- 1326). The diffraction peak at 2θ = 43.27 has been found to shift towards left for the thermally treated samples. The SEM and AFM analysis reveals the size of agglomerated copper spheroids to lays between 400nm to 1µm and each agglomerate containing nano sized (20–30) nm copper spheroids. After DSC scan the small grains of the deposits are found to be 100 to 200 nm size on very large grains.

References

1. Mararka S. P., Gutmann R. J., Advanced multilayer metallization schemes with copper as interconnection metal, Thin Solid Films., 236 (1993): pp. 257-266
2. Zhang J. M., Xu K. W., Ji V., Competition between surface and strain energy during grain growth in free-standing and attached Ag and Cu films on Si substrates, Applied Surface Science., 187 (2002): pp. 60-67
3. Anderson J. C., Applications of thin films in microelectronics, Thin Solid Films., 12 (1972): pp. 1-15
4. Granneman E. H. A., Thin films in the integrated circuit industry: requirements and deposition methods, Thin Solid Films., 228 (1993): pp. 1-11
5. Yin K. B., Xia Y.D., Chan C. Y., Zhang W. Q., The kinetics and mechanism of room-temperature microstructural evolution in electroplated copper foils, Scripta Materialia., 58 (2008): pp. 65-68
6. Harper M. E., Cabra C., Andricacos P. C., Gignac L., Noyan I. C., Mechanisms for microstructure evolution in electroplated copper thin films near room temperature, Journal of Applied Physics., 86 (1999): pp. 2516-2525
7. Wang h., Huang Y., Tan Z., Hu X., Fabrication and characterization of copper nanoparticle thin films and the electrocatalytic behavior, Analytica Chimica Acta., 526 (2004): pp. 13-17
8. Podaha E. J., Selective Electrodeposition of Nanoparticulates into Metal Matrices, Nano Letters., 1 (2001): pp. 413-416
9. Ibanez A. Fatas E., Mechanical and structural properties of electrodeposited copper and their relation with the electrodeposition parameters, Surface and Coatings Technology., 191 (2005): pp. 7-16
10. Wijesundera R. P., Hidaka M., Koga K., Sakai M., Siripala W., Growth and characterization of potentiostatically electrodeposited Cu_2O and Cu thin films, Thin Solid Films., 500 (2006): pp. 241-246

11. Chatterjee A. P., Mukhopadhyay A. K., Chakraborty A. K., Sasmal R. N., Lahiri S. K., Electrodeposition and characterization of cuprous oxide films, Materials Letters., 11 (1991): pp. 358-362
12. Mirkin M. V., Nilov A. P., Three dimensional nucleation and growth under controlled potential, Journal of Electroanalytical Chemistry., 283 (1990): pp. 35-51.
13. Ratsch C., Venables J. A., Nucleation theory and the early stages of thin film growth, Journal of Vacuum Science and Technology. A., 21 (2003): pp. S96-S109
14. Schmelzer J. W. P., Comments on the Nucleation Theorem, Journal of Colloid and Interface Science., 242 (2001): pp. 354-372
15. Grujicic D., Pesic B., Electrodeposition of copper: The nucleation mechanisms, Electrochimica Acta., 47 (2002): pp. 2901-2912
16. Venables J. A., Spiller G. D. T., Hanbucken M., Nucleation and growth of thin films, Reports on Progress in Physics., 47 (1984): pp. 399-459
17. Budevski E., Staikov G., Lorenz W. J., Electrocrystallization Nucleation and growth phenomena, Electrochimica Acta., 45 (2000): pp. 2559-2574.
18. Scarifker B., Hills G., Theoritical and Experimental Studies of Multiple Nucleation, Electrochimica Acta., 28 (1983): pp. 879-889
19. Zainal Z., Kassim A., Hussein M. Z., Ching C. H., Effect of bath temperature on the electrodeposition of copper tin selenide films from aqueous solution, Materilas Letters., 58 (2004): pp. 2199-2202
20. Fenineche N., Coddet C., Saida A., Effect of electrodeposition Parameters on the microstructure and Mechanical properties of Co-Ni Alloys, Surface and Coatings Technology., 41 (1990): pp. 75-81
21. Dulal S. M. S. I., Yun H. J., Shin C. B., Kim C. K., Electrodeposition of CoWP film. Effect of pH and temperature, Electrochimica Acta., 53 (2007): pp. 934-943
22. Ruiz A. M., Pardave M. P., Batina N., Overpotential deposition of copper on an iodine-modified Au (111) electrode, Electrochimica Acta., 53 (2008): pp. 2115-2120
23. Ramirez C., Arce E. M., Romo M., Pardave M. P., The effect of temperature on the Kinetics and mechanism of silver electrodeposition, Solid State Ionics., 169 (2004): pp. 81-85
24. Cheng W. B., Hua Z. J., Influence of Ultrasonic Cavitation on passive film of Stainless steel, Ultrasonics Sonochemistry., 15 (2008): pp. 239-243

25. Patil M. N., Pandit A. B., Cavitation-A novel technique for making stable nano-suspensions, Ultrasonic Sonochemistry., 14 (2007): pp. 519-530
26. Chow R., Blindt R., Chivers R., Povey M., A study on the primary and secondary nucleation of ice by power ultrasound, Ultrasonics., 43 (2005): pp. 227-230
27. Doktycz S. J., Suslik K. S., Interparticle Collisions Driven by Ultrasound, Science., 247 (1989): pp. 1067-1069
28. Arrojo S., Benito Y., A theoretical study of hydrodynamic cavitation, Ultrasonic Sonochemistry., 15 (2008): pp. 203-211
29. Hyde M. E., Compton R. G., How Ultrasound influences the electrodeposition of metals., Journal of Electroanalyical Chemistry., 531 (2002): pp. 19-24
30. Gedanken A. Using sonochemistry for the fabrication of nanomaterials, Ultrasonics Sonochemistry., 11 (2004): pp. 47-55
31. Cain P. W., Martin P. D., Price C. J., The use of ultrasound in industrial chemical synthesis and crystallization1. Applications to synthetic chemistry, Organic Process Research and Development., 2 (1998): pp. 34-48
32. Ghasemi S., Mousavi M. F., Shamsipur M., Karami H. Sono chemical-assisted synthesis of nano-structured lead dioxide, Ultrasonics Sonochemistry., 15 (2008): pp. 448-455
33. Gedanken A., Using sonochemistry for the fabrication of nanomaterials, Ultrasonics Sonochemistry., 11 (2004): pp. 47-55
34. Hamid Z., Ghayad I. M., Characteristics of electrodeposition of Ni-polyethylene composite coatings, Materials Letter., 53 (2002): pp. 238-243
35. Zhang Y. W., Bower A. F., Xia L., Shih C. F.,Three dimensional finite element analysis of the evolution of voids and thin films by strain and electromigration induced surface diffusion, Mechanics and Physics of Solids., 47 (1999): pp. 173-199
36. Pierce D. G., Brusius P. G., Electromigration: A Review, Microelectrone Reliability., 37 (1997): pp. 1053-1072
37. Kwon D., Park H., Lee C., Electromigration resistance-related microstructural change with rapid thermal annealing of electroplated copper films, Thin Solid films., 475 (2005): pp. 58-62
38. Seker E., Reed M. L., Begley M. R., A thermal treatment approach to reduce microscale void formation in blanket nanoporous gold films, Scipta Materialia., 60 (2009): pp. 435-438

39. Dutta I., Park C., Vella J., Effect of internal stresses on thermo-mechanical stability of interconnect structures in microelectronic devices, Materials Science and Engineering A., 421 (2006): pp. 118-132
40. Yu H., Hutchinson. J. W., Delamination of thin film strips, Thin Solid Films., 423 (2003): pp. 54-63
41. Kriese M. D., Moody N. R., Gerberich W. W., Effects of Annealing and interlayers on the adhesion energy of copper thin films to SiO_2/Si substrates, Acta materilia., 46 (1998): pp. 6623-6630
42. Lee A., Clemens B. M., Nix W. D., Stress induced delamination methods for the study of adhesion of Pt thin films to Si. Acta Materialia 52(2004): pp. 2081-2093
43. J. M. E. Harper, C. Cabral, P. C. Andricacos, L. Gignac, I. C. Noyan. Mechanisms for microstructure evolution in electroplated copper thin films near room temperature. Journal of applied physics. 86 (1999) 2516-2525.
44. K. B. Yin, Y.D. Xia, C. Y. Chan, W. Q. Zhang. The Kinetics and mechanism of room-temperature microstructural evolution in electroplated copper foils. Scripta Materialia. 58 (2008) 65-68.
45. W. Dong, J. Zhang, J. Sheng. Self-annealing of electrodeposited copper thin film during room temperature storage. Materials Letters. 62 (2008) 1589-1591
46. Chambers R. G., Proc. R. Soc. London, Ser. A., 202 (1950): pp. 378
47. Patten J. W., Mcclanahan E. D., Johnston J. W., Room-temperature Recrystallization in thick Bias-Sputtered Copper deposits, Journal of Applied Physics., 42 (1971): pp. 4371-4377
48. Thompson C. V., Carel R., Stress and grain growth in thin Films, Journal of Mechanics and Physics of Solids., 44 (1996): pp. 657-673
49. Chaudhari P., Grain growth and Stress Relief in Thin Film. Journal of Vacuum Science and Technology., 9 (1971): pp. 520-522
50. Lucel F. P., Fichtner P. F. P., Schelp L. F., Zawislak F. C., Abnormal Gain Growth Behavior in Nanostructured Al Thin Films on SiO2/Si Substrates, Mater. Res. Soc. Symp. Proc., 1150 (2009): pp. RR06-03
51. Zhou L. Z., Gou J. T., Grain Growth and Kinetics for Nanocrystalline NiAl, Scripta Materialia 40 (1999): pp. 139-144

52. Huang M., Wang Y., Chang Y. A., Grain growth in sputtered nanoscale PdIn thin films, Thin Solid Films., 449 (2004): pp. 113-119
53. Thompson C. V., Grain Growth in Thin Films, Annu. Rev. Mater. Sci., 20 (1990): pp. 245-268
54. Mullin W.W., The effect of thermal grooving on grain boundary motion, Acta Metallurgica., 6 (1958): pp. 414-427
55. Ch'ng H. N., Pan. J., Sintering of particles of different sizes, Acta Materialia., 55 (2007): pp. 813-824
56. Detavernier C., Rossnagel S., Noyan C., Guha S., Cabral C., Lavoie C., Thermodynamics and kinetics of room-temperature microstructural evolution in copper films, Journal of Applied Physics., 94 (2003): pp. 2874-2881
57. Finsy R., On the critical radius in Ostwald ripening, Langmuir., 20 (2004): pp. 2975-2976
58. http://en.wikipedia.org/wiki/Ostwald_ripening 26.05.10
59. Madras G., Coy B. J., Continuous distribution theory for Ostwald ripening: comparison with LSW approach, Chemical Engineering Science., 58 (2003): pp. 2903-2909
60. Qin-bo W., Finsy R., Hai-bo X., Xi L., On the critical radius in generalized Ostwald ripening, Journal of Zhejiang University Science., 8 (2005) 705-707
61. Singh V., Physical Metallurgy. Delhi, Standard Publishers, 1999
62. Lee S. Y., Choi S. H., Park C. O., Oxidation, grain growth and reflow characteristics of copper thin film prepared by CVD, Thin Solid films., 359 (2000): pp. 261-267
63. Perananthan P., Jeyachandran Y. L., Viswanathan C., N.N. Praveena, P.C. Chitra, D. Manglaraj, Narajandass S. K., The effect of annealing on vacuum-evaporated copper selenide and indium telluride thin films. Materials Characterization 58 (2007): pp. 756-764
64. Admon U., Dahan I., Dariel M.D., Kimmel G., Sariel J., Copper grain growth in thin film Cu-Cr multilayers, Thin Solid Films., 251 (1994): pp. 105-109
65. Sharma S.K., Spitz J., Hillock formation, hole growth and agglomeration in thin silver films, Thin Solid Films., 65 (1980): pp. 339-350
66. Mohanty B. C., Kasiviswanathan S., Thermal stability of silver selenide thin films on silicon formed from the solid state reaction of silver and selinide films, Thin Solid films., 515 (2006): pp. 2059-2065

67. Ramos A. S., Vieira M. T., Duarte L. I., Vieira M. F., Viana F., Calinas R., Nanometric multilayers: A new approach for joining TiAl, Intermetallics., 14 (2006): pp. 1157-1162
68. Vovk V., Schmitz G., Kirchheim R., Three dimentional atom probe investigation of Co/Al thin film reaction, Microelectronic Engineering. 70 (2003): pp. 533-538
69. Klement U., Erb U., El-nSherik A. M., Aust K.T., Thermal stability of nanocrystalline Ni, Material Science and Engineering. A., 203(1995): pp. 177-186
70. Ma D., Chi D. Z., Loomans M. E, Wang W. D., Kinetics of NiSi-to-$NiSi_2$ transformation and morphology evolution in nickel silicide thin films on Si, Acta Materialia., 54 (2006): pp. 4905-4911
71. Fisher J. M., Berlouis L. E. A., Sawer L. J. M., Growth Charaterization of electrodeposited films of cadmium telluride on Silicon, Journal of crystal growth., 138 (1994): pp. 86-93
72. Hua M. Y., Tsai R. Y., Crystallization kinetics of electrodeposited amorphous ($CrC_{0.18}$) films studied by DSC, Thin Solid Films., 388 (2001): pp. 165-170
73. Douglas G., Birkin P. R., Leighton T. G., Electrodeposition of copper in presence of an acoustically excited gas bubble, Electrochemistry Communications., 9 (2007): pp. 1062-1068
74. Samuel H. G.; Ultrathin Films and Interfacial Phenomena- Comparison of Different Molecular Organization Processes; Doctoral dissertation, University of Saskatchewan Saskatoon, 2003.
75. Rassaei L.; Assembly and Characterization of Nanomaterials into Thin Film Electroanalysis; Doctoral dissertation, University of Kuopio, Kuopio, 2008.
76. Khelladi M.R, Mentar L, Azizi A, Sahari A, Kahoul A.; Electrochemical Nucleation and growth of copper deposition onto FTO and n-Si(100) electrodes; Materials Chemistry and Physics, 115 (2009): pp 385-390.
77. Grujicic D., Pesic B., Electrodeposition of copper: the nucleation mechanisms, Electrochimica Acta., 47 (2002): pp. 2901-2912
78. http://www.google.co.in/images?hl=en&q=Xray%20diffraction%20principle&safe=active&um=1&ie=UTF-8&source=og&sa=N&tab=wi/16.05.10
79. http://serc.carleton.edu/research_education/geochemsheets/techniques/SEM.html/16.05.10http://en.wikipedia.org/wiki/Scanning_electron_microscope/16.05.10

80. http://en.wikipedia.org/wiki/Atomic_force_microscopy/16.05.10
81. http://en.wikipedia.org/wiki/Differential_scanning_calorimetry 26.05.10
82. http://en.wikipedia.org/wiki/Contact_angle 26.05.10
83. Mallik A., Bankoti A., Ray B. C., A study on the Modification of Conventional Electrochemical Crystallization under Sonication: The Phenomena of Secondary Nucleation, Electrochemical and Solid State Letters., 12 (2009): pp. F46-F49
84. Lei Y. C., Cai W., An X., Gao L. X., The effect of the underlying substrate on crystallization kinetics of TiNi thin films, Journal of Non-crystalline Solids., 354 (2008): pp. 4572-4576
85. Kissinger H. E., Reaction Kinetics in Differential Thermal Analysis, Analytical Chemistry., 29 (1957): pp. 1702-1706
86. Lu K., Wei W. D., Wang J. T., Grain growth kinetics and interfacial energies in nanocrystalline Ni-P alloys, Journal of Applied Physics., 69 (1991): pp. 7345-734
87. Chen J. Z., Wu S. K., Crystallization behavior of r.f. sputtered Ti Ni thin films, Thin Solid Films., 339 (1999): pp. 194-199
88. Rajagopalan T., Reddy G. B., Effect of annealing rate on the crystallization process in $Ge_5Bi_{18}Se_{77}$ films, Thin Solid Films., 353 (1999): pp. 254-258
89. Dannenberg R., Stach E. A., Grozac J. R., Dresser B. J., In-situ TEM observations of abnormal grain growth, coarsening, and substrate de-wetting in nanocrystalline Ag thin films, Thin Solid Films., 370 (2000): pp. 54-62
90. Yoo C. S., Cynn H., Nicol M. F., Elementary Reactions of Nitrogen and Oxygen with Boron and Carbon at High pressures and temperatures, International Conference on High pressure Science and Technology, Kyoto, Japan, August 25-29, 1997
91. Cullity B. D., Elements of X-Ray Diffraction, Addision-Wesley Publisher., MA, 1978
92. International Committee for Diffraction Data: Card No. 01-085-1326